# Evaluating the carbon and nitrogen cycles of the QUINCY terrestrial biosphere model using space-born optical remotely-sensed data

Tuuli Miinalainen<sup>1,2,3</sup>, Amanda Ojasalo<sup>1,4</sup>, Holly Croft<sup>5</sup>, Mika Aurela<sup>2</sup>, Mikko Peltoniemi<sup>6</sup>, Silvia Caldararu<sup>7</sup>, Sönke Zaehle<sup>3</sup>, and Tea Thum<sup>2</sup>

**Correspondence:** Tuuli Miinalainen (tuuli.miinalainen@fmi.fi)

Abstract. Accurate estimates of future land carbon sinks and thus the remaining carbon budget to achieve the Paris climate goals requires rigorous modelling of the carbon sequestration potential of the terrestrial biosphere. Estimating the terrestrial carbon budget requires an accurate understanding of the interlinkages between the land carbon and nitrogen cycles, yet coupled carbon-nitrogen cycle models exhibit large uncertainties. Leaf chlorophyll, chl<sub>leaf</sub>, is an indicator of the leaf nitrogen content stored within photosynthetic nitrogen pools and is central to the exchange of carbon, water and energy between the biosphere and the atmosphere. In this work, we harness an advanced remote sensing (RS) chl<sub>leaf</sub> product to evaluate a terrestrial biosphere model, QUantifying Interactions between terrestrial Nutrient CYcles and the climate system (QUINCY), which explicitly models chl<sub>leaf</sub>. We focus on comparing the spatial and seasonal patterns of modelled and observed chl<sub>leaf</sub>, and then further assessing if modelled leaf area and productivity agree with a RS leaf area index product and in-situ eddy covariance-based gross primary production, respectively. In addition, we conduct additional simulations to test two alternative formulations of leaf-internal nitrogen allocation within QUINCY. Our analysis over a globally representative set of locations reveals that QUINCY chl<sub>leaf</sub> magnitudes are mostly in line with the RS chl<sub>leaf</sub> values. However, QUINCY chl<sub>leaf</sub> tends to show a narrower numerical range compared to RS for specific ecosystem types, such as grasslands. While the seasonal cycle of QUINCY chl<sub>leaf</sub> mostly corresponds well to the observations, for many deciduous forests, the increase in QUINCY's chl<sub>leaf</sub> predictions in spring and the decrease in autumn were delayed compared to observations. Our results also show that compared to the original leaf nitrogen allocation scheme of QUINCY, the revised scheme produced a more reasonable sensitivity of gross primary production to increases in chleaf. However, the revised scheme did not directly lead to improvement in simulating chl<sub>leaf</sub> and gross primary production. Our study shows the value of RS products linked to N cycle that will be useful in both  $\leftarrow$ and N carbon and nitrogen modelling, and paves way for closer linking of RS and TBMs.

<sup>&</sup>lt;sup>1</sup>Earth Observation Research, Finnish Meteorological Institute, P.O. Box 503, 00101 Helsinki, Finland

<sup>&</sup>lt;sup>2</sup>Climate System Research, Finnish Meteorological Institute, P.O. Box 503, 00101 Helsinki, Finland

<sup>&</sup>lt;sup>3</sup>Department of Biogeochemical Signals, Max Planck Institute for Biogeochemistry, Hans-Knöll-Straße 10, 07745 Jena, Germany

<sup>&</sup>lt;sup>4</sup>Department of Geosciences and Geography, University of Helsinki, Gustaf Hällströmin katu 2, 00560 Helsinki, Finland

<sup>&</sup>lt;sup>5</sup>School of Biosciences, University of Sheffield, Western Bank, Sheffield, S10 2TN, United Kingdom

<sup>&</sup>lt;sup>6</sup>Natural Resources Institute Finland (Luke), Latokartanonkaari 9, 00790 Helsinki, Finland

<sup>&</sup>lt;sup>7</sup>Discipline of Botany, School of Natural Sciences, Trinity College Dublin, College Green, Dublin 2, Ireland

#### 1 Introduction

The terrestrial biosphere currently takes up approximately one-third of the anthropogenic fossil fuel carbon emissions (Friedling-stein et al., 2023), and thereby playing pivotal role in slowing global climate warming (Nabuurs et al., 2022). The Carbon (C) cycle is closely linked to the terrestrial nitrogen (N) cycle, as photosynthesis and plant growth require sufficient nutrient supply. Land carbon uptake is limited by nitrogen in many ecosystems (LeBauer and Treseder, 2008; Fisher et al., 2012; Tamm, 1991; Vitousek and Howarth, 1991; Ziehn et al., 2021), however, the magnitude of this limitation remains unclear. This highlights the need to better understand the coupled C and N cycles (Seiler et al., 2024), as future changes in climate will also affect these cycles (Arora et al., 2020).

Terrestrial biosphere models (TBMs) can be used to simulate coupled C and nutrient cycles and land-atmosphere interactions under a changing climate. In recent decades, TBMs have taken in an increasing number of factors affecting plant photosynthesis, such as nutrient limitation (Blyth et al., 2021). Whilst Kou-Giesbrecht et al. (2023) reported that TBMs are capable of reproducing the historical terrestrial C sink with a sufficient level of performance, uncertainties persist. For example, models have varying methods to represent the N-limitation of photosynthesis, which can lead to different results for plant productivity (Medlyn et al., 2015). TBMs use different modeling approaches to represent N limitation of photosynthesis and the effect of N availability on leaf N, which can lead to varying results regarding plant productivity (Medlyn et al., 2015). Leaf N can be obtained directly from soil N availability by using a fixed parameter or with flexible parametrization using leaf C:N ratios (Thomas et al., 2015). Increasing model complexity regarding modeling the N limitation can thereby also introduce further uncertainties into the estimates of the carbon sink (Fisher and Koven, 2020; Famiglietti et al., 2021), which is through both process and parameter uncertainty, given the inclusion of new process equations. These uncertainties are also reflected in significant divergence of N pools and fluxes predicted modelled by the current generation of TBMs (Kou-Giesbrecht et al., 2023). In addition, the modelled responses of photosynthesis to elevated atmospheric carbon dioxide (CO<sub>2</sub>) or to N deposition vary between different TBMs, requiring a better understanding of the N cycle (Davies-Barnard et al., 2020; Arora et al., 2020; Meyerholt et al., 2020; Zaehle et al., 2014). It is therefore important to better constrain the nitrogen dynamics in these models. One of the major sources of uncertainty in modeling the land carbon sink with TBMs is the uncertainty in estimating the leaf photosynthetic capacity and photosynthetic rate (Bonan et al., 2011; Rogers et al., 2017). Leaf chlorophyll (chl<sub>leaf</sub>) is intrinsically related to plant photosynthesis, due to its role in generating biochemical energy for the carboxylation reactions within the Calvin-Benson cycle, through the harvesting of solar radiation. Previous work has demonstrated that leaf chlorophyll content is a strong proxy for photosynthetic capacity (Croft et al., 2017; Lu et al., 2020; Luo et al., 2021). The maximum carboxylation rate at the 25  $^{\circ}$ C reference temperature ( $V_{c(max),25}$ ) represents the limitation of photosynthesis by the Rubisco enzyme, which is the main regulator in light-saturated photosynthesis (Houborg et al., 2013). Due to the investment of N in chl<sub>leaf</sub> molecules and an optimal N investment strategy to ensure close co-ordination between light-harvesting and carboxylation reactions, there is a close relationship between leaf N and chl<sub>leaf</sub> (Sage et al., 1987; Evans, 1989). In-situ observations of chl<sub>leaf</sub> can therefore be used to improve the parametrization of physiological schemes within TBMs to improve GPP estimates (Luo et al., 2018, 2019; Lu et al., 2022; Thum et al., 2025). However, many of the contemporary TBMs do not represent chl<sub>leaf</sub>, and the widely used version of the FvCB model (Farquhar et al., 1980) for photosynthesis description does not explicitly take into account the role of chl<sub>leaf</sub> in photosynthesis. In addition, the majority of TBMs only consider total canopy N and its vertical distribution (Krinner et al., 2005; Best et al., 2011; Clark et al., 2011) (Vuichard et al., 2019; Best et al., 2011; Clark et al., 2011).

In addition to *in-situ* observations, remote sensing (RS) of the Earth's vegetation provides comprehensive data for evaluating and validating TBMs. Leaf nitrogen is difficult to retrieve directly from RS observations (Farella et al., 2022), in comparison to chl<sub>leaf</sub> which is more feasible to derive remotely (Croft and Chen, 2018), due to the presence of large chlorophyll absorption features in visible wavelengths. The advantage of using remotely sensed chl<sub>leaf</sub> is its global and seasonal coverage and relatively long time span, compared to *in-situ* observations. Similarly as *in-situ* observations, RS chl<sub>leaf</sub> can be harnessed to improve the modeled photosynthetic processes which include  $V_{c(max)}$  (Houborg et al., 2013). For example, Liu et al. (2023) retrieved global daily  $V_{c(max)}$  for C3 biomes by using RS chl<sub>leaf</sub> and RS solar-induced chlorophyll fluorescence. Another advantage of RS chl<sub>leaf</sub> is that they are linked to space-borne observations of leaf area index (LAI), both retrievable remotely (Croft et al., 2020). This allows the modeled leaf surface area to be evaluated simultaneously with chl<sub>leaf</sub>.

In this study, we utilized a spatial RS  $chl_{leaf}$  product (Croft et al., 2020) to evaluate the  $chl_{leaf}$  representation of the TBM QUINCY (QUantifying Interactions between terrestrial Nutrient CYcles and the climate system) (Thum et al., 2019; Caldararu et al., 2020), which has fully prognostic coupled carbon and nitrogen cycles. QUINCY includes an explicit representation of  $chl_{leaf}$  and its impact on photosynthesis, and also the photosynthetic parameters  $V_{c(max),25}$  and the maximum electron transport rate at 25 °C reference temperature ( $J_{max,25}$ ) are directly determined from leaf nitrogen. We analysed model performance with respect to the temporal and spatial distribution of  $chl_{leaf}$  and LAI in different ecosystems globally. We further compared the simulated gross primary production (GPP) with the ground-based measurement from eddy-covariance network stations. To understand model-data mismatch, we used a machine learning approach to analyze how different environmental drivers affect both QUINCY and RS  $chl_{leaf}$ . We further investigated whether the observed difference in  $chl_{leaf}$  between QUINCY and observations is related to modeled N limitation by examining QUINCY's leaf C:N values. Here we use RS data as a reference for evaluation, though we acknowledge that RS data are also simulated product and have different characteristics than *in-situ* data. In other words, our evaluation can be understood more as a comparison study between TBM and RS-derived data.

Initial results suggested that the <u>modeled</u> response of  $chl_{leaf}$  to leaf N was not realistic, foremost because the original leaf nitrogen scheme in QUINCY does not take into account of the observed relationship between <u>chlorophyll and V<sub>c(max)</sub></u> (Evans and Clarke, 2019). In order to have a more realistic representation, we formulated an alternative leaf N allocation scheme in QUINCY based on Onoda et al. (2017) and <u>Evans and Clarke (2018)</u> Evans and Clarke (2019), where the V<sub>c(max)</sub> and <u>chlorophyll chl<sub>leaf</sub></u> ratio is taken into account, and compared the additional simulation results with the original leaf N allocation scheme.

The objectives of the study were to determine different methods for using RS  $chl_{\rm leaf}$  in model evaluation and how RS  $chl_{\rm leaf}$  can benefit modeling of coupled C and N cycles. The research questions addressed in this work are as follows:

- Are the spatial and temporal patterns of global chl<sub>leaf</sub> in QUINCY and RS similar?

85

- Is QUINCY's performance in modeling chl<sub>leaf</sub> related to its ability to produce measured annual GPP?
- What are the main environmental drivers that affect QUINCY chl<sub>leaf</sub> and RS chl<sub>leaf</sub>?

#### 90 2 Materials and methods

In this section, we will first present the  $\frac{\text{QUINCY model study sites}}{\text{Multiple study sites}}$  and observational data<del>used in the study</del>, followed by the study sites  $\frac{\text{QUINCY model description}}{\text{QUINCY model description}}$  and simulation setup. Finally, a machine learning approach to determine  $\frac{\text{chl}_{leaf}}{\text{chl}_{set}}$  denotes both chlorophyll a and b  $\frac{\text{chl}_{a+b}}{\text{chl}_{set}}$ . All the datasets used in the study are presented in Table S1.

# 95 **2.1 Description of the sites**

We conducted the analysis using two different site sets. The first set was the Protocol for the Analysis of Land Surface Models (PALS) Land Surface Model Benchmarking Evaluation Project (PLUMBER2) (Ukkola et al., 2022). The second site set, GLOBAL, is based on the study by Caldararu et al. (2022).

PLUMBER2 (Abramowitz et al., 2024) was designed for serving in a model intercomparison project for land surface models, and provides CO<sub>2</sub> eddy covariance measurements and meteorological data for various sites. The time interval of PLUMBER2 site data varies depending on the site, as some of the site data cover only one year, while others over a decade. The time span of PLUMBER2 site data is between 1992–2018. Of the available sites, we included 143 PLUMBER sites that had RS chl<sub>leaf</sub>, RS LAI and QUINCY data available, and that were not reported by Abramowitz et al. (2024) to have anomalous precipitation input data. The GLOBAL site set represents all major climate zones and global biomes, and the site input data is for the years 1989–2018 based on the CRU JRA dataset (Harris, 2020). In our analysis, we used 279 GLOBAL sites for which QUINCY simulated and RS chl<sub>leaf</sub> data were available and matched in land cover type (See Section 2.2.3).

In total, the combined PLUMBER2 and GLOBAL analysis included 422 sites. The locations of the PLUMBER2 and GLOBAL sites are presented in Fig. S1. The sites are categorized based on the QUINCY plant functional types (PFTs), and the number of GLOBAL and PLUMBER2 sites in each PFT are listed in Table 1.

# 110 2.2 Remote sensing data

# 2.2.1 Remotely sensed chlleaf

MERIS full-resolution reflectance data with a two-stage radiative transfer model. The spatial resolution of the global RS chl<sub>leaf</sub> is 300 m, and the data are processed to a 7-day temporal resolution for the years 2003–2011. The chl<sub>leaf</sub> has been retrieved by

first modeling the reflectance spectra at the leaf level using two separate models: the 4-Scale model (Chen and Leblanc, 1997) for forested and spatially clumped ecosystems, and the SAIL model (Verhoef, 1984) for cropland and grassland ecosystems.

The chl<sub>leaf</sub> has been then derived from the leaf reflectance spectra by using the PROSPECT leaf optical model (Jacquemoud and Baret, 1990).

We obtained chl<sub>leaf</sub> content from the global RS product by Croft et al. (2020). The RS chl<sub>leaf</sub> is derived from the ENVISAT

Table 1. List of QUINCY PFTs and the corresponding number of sites in the PLUMBER2 and GLOBAL site sets

Abbreviation	Long name	Nr of sites, PLUMBER2	Nr of sites, GLOBAL	Nr of sites, all
BNE	Boreal needle-leaved evergreen	20	50	<del>70</del>
<u>TeNE</u>	Temperate needle-leaved evergreen	8	<u>6</u>	<u>14</u>
<u>BNS</u>	Boreal needle-leaved deciduous	$\widetilde{0}$	<u>6</u> €	<u>6</u>
<u>TeBE</u>	Temperate broad-leaved evergreen	$\stackrel{4}{\sim}$	4_	8
<u>TeBS</u>	Temperate broad-leaved deciduous	25	20	<u>45</u>
<u>TrBR</u>	Tropical broad-leaved rain deciduous	2~	2_	4 €
<u>TrBE</u>	Tropical broad-leaved evergreen	9_	38	<u>47</u>
<u>TeC</u>	C3 crops	21	0_	21
₹eH	C3 grasslands	<u>34</u>	<u>69</u>	103
<u>TrH</u>	C4 grasslands	20	<u>84</u>	104
all	- -	143	279	<u>422</u>

. The influence of gaps has been partially minimized in the RS  $chl_{leaf}$  by Croft et al. (2020) by gap-filling the missing data with the year 2010 data and a smoothing algorithm. A detailed description of the RS  $chl_{leaf}$  product is presented in Croft et al. (2020)

In addition, we obtained chlorophyll content data based on the Sentinel-3 OLCI data (Reyes-Muñoz et al., 2022) for two needle-leaved sites for which we also had *in-situ* chl<sub>leaf</sub> measurements (See Section 2.3.2). The RS chl<sub>leaf</sub> product by Reyes-Muñoz et al. (2 is generated by involving Gaussian process regression algorithms, and the training data for the algorithm consisted of simulated top of atmosphere radiance from coupled canopy radiative transfer model SCOPE and the atmospheric radiative transfer model 6SV. The aim was to further evaluate the magnitude and the seasonality of chl<sub>leaf</sub> for the needle-leaved evergreen boreal forests by using data from a different Earth observation instrument and also obtained with a different retrieval algorithm than with RS chl<sub>leaf</sub> by Croft et al. (2020).

# 2.2.2 Remotely sensed LAI

120

We used the GEOV1 remotely-sensed leaf area index (LAI) product from the Copernicus Global Land Service (Baret et al., 2013), which is the same RS LAI product used to retrieve the RS chl<sub>leaf</sub> by Croft et al. (2020). GEOV1 LAI is derived from the SPOT-VGT satellite data and has a temporal resolution of ten days and a spatial resolution of 1 km. We used data for the years 2003–2011.

#### 2.2.3 Post-processing of the RS data

As RS chl<sub>leaf</sub> depends in part on the assumed land cover (LC) type for each grid cell, it was important to ensure that the

QUINCY chl<sub>leaf</sub> values for each site represented the same ecosystems as RS chl<sub>leaf</sub>. We compared the PFT values used in the

QUINCY simulations with the LC values from a European Space Agency Climate Change initiative (ESA-CCI-LC) LC map

(ESA, 2017), from which the LC types were also taken for the RS chl<sub>leaf</sub> retrieval modeling by Croft et al. (2020). A list of LC types is presented in Table S2, and the LCs associated with each PFT in our comparison are presented in Table S3. For each site, we first selected the site grid cell and the eight surrounding grid cells, i.e. the 3x3 cell area, from the ESA-CCI LC map.

We then checked whether the QUINCY PFT matched the LC type for each of the grid cells, and added to a list those grid cells that had a matching land cover type to the QUINCY PFT. We then picked from the RS chl<sub>leaf</sub> grid data only those listed grid cells that had a matching land cover type, and calculated an area average RS chl<sub>leaf</sub> based on the listed cells. This area average was calculated separately for each time step. If there were no matching grid cells in the 3x3 surrounding cells, we extended the search to cover 5x5 surrounding cells, and looped through 25 grid cells. We then selected the matching cells from the 25 cells, and calculated the area average RS chl<sub>leaf</sub> for each time step. There were eight PLUMBER2 sites and 80 GLOBAL sites for which we did not find any matching grid cells, and these sites were excluded from the analysis. We only used the top-of-canopy chl<sub>leaf</sub> values from QUINCY to ensure that the values were consistent with the RS-based values. In addition, the RS chl<sub>leaf</sub> for the needle-leaved sites was multiplied by  $\frac{\pi}{2}$ . This was done to account for the half-hemispherical needle geometry in the remote sensing retrieval (Stenberg et al., 1995).

The RS LAI data were only retrieved using the one grid cell where the site was located, i.e. the PFT classification of a site did not affect the RS LAI post-processing. If no data were available in that particular grid cell, we extended the area to cover  $\pm 0.01^{\circ}$  latitude and longitude degrees and used the average of the whole extended area.

## 2.3 *In-situ* observations

150

## 2.3.1 Eddy covariance flux observations

Ground station GPP observations were available for the PLUMBER2 sites, and the data were taken from the eddy covariance flux tower dataset provided by Ukkola et al. (2022). The dataset includes flux tower data from three data releases: FLUXNET2015 (Pastorello et al., 2020), La Thuile (FLUXNET, 2024), and OzFlux (Isaac et al., 2017). The flux data were gap-filled using statistical methods depending on the length of the gap. The short gaps up to four hours were gap-filled using linear interpolation methods. Gaps that were longer than four hours were gap-filled with linear regression against the incoming shortwave (SW)
 radiation, air temperature and humidity, or only against the SW radiation if the other two variables were missing. Depending on the site, the flux time series ranged from one to 20 years, between the years 1992 and 2018 (See Ukkola et al. (2022) Table S1). Data from all years were used, and therefore, the GPP time series are not necessarily from the same time interval as RS chl<sub>leaf</sub>.

# 2.3.2 chl<sub>leaf</sub> and leaf C:N in-situ measurements

To further investigate the chl<sub>leaf</sub> magnitude and seasonal cycle for boreal needle-leaved evergreen (BNE) forests, we performed an additional comparison for RS and QUINCY output with *in-situ* observations for two PLUMBER2 sites: Sodankylä site (FI-Sod) in Finland (67.4 °N, 26.6 °E) (Thum et al., 2007) and Niwot Ridge (US-NR1) in the United States (40.0 °N, -105.5 °E) (Bowling and Logan, 2019). Both sites are characterized as needle-leaved forest sites with strong seasonal cycle and harsh

winters. FI-Sod is classified as boreal forest, and US-NR1 as subalpine, and it is located in a mountainous terrain. The sites were selected as both sites had a time series of chl<sub>leaf</sub> observations. In addition, there were also fraction of absorbed photosynthetic radiation (fAPAR) *in-situ* observations available at FI-Sod, which we used in our analysis. Further details about chl<sub>leaf</sub> data collection and the use of *in-situ* observations is provided in Text S1.

We also used *in-situ* observations from the TRY database (Kattge et al., 2011) to compare the *in-situ* leaf C:N ratios with our model-derived values. The leaf C:N observations were retrieved from the TRY database for two sites: the boreal needle-leaved forest station Hyytiälä in Finland (FI-Hyy, 61.8°N, 24.3°E) and the deciduous forest site, Morgan Monroe State Forest site in the US (US-MMS, 39.3°N, -86.4°E). The FI-Hyy measurements are sampled from Scots pine tree. US-MMS is a secondary successional broad-leaved forest, and the leaf C:N measurements cover various different deciduous trees: sugar maple (*acer saccharum*), American beech (*fagus grandifolia*), American elm (*Ulmus americana*), Northern red oak (*Quercus rubra*), and other deciduous species. The sites were selected based on consistent measurement time with the QUINCY simulations, and to expand the geographical gradient of *in-situ* measurements, and also to include an example of a TeBS site.

# 2.4 Terrestrial biosphere model QUINCY

170

175

180

185

195

200

We used the terrestrial biosphere model QUINCY (Thum et al., 2019), which includes fully coupled carbon, nitrogen and phosphorus (P) cycles, as well as water and energy fluxes in ecosystems. Global vegetation ecosystems are classified into eight categories by plant functional types (PFTs)PFTs. In addition, there are several acclimation mechanisms that allow a smooth transition of ecosystem functioning in different climatic conditions. Vegetation is represented as an average individual, which is characterised by its height and diameter as well as an average individual density, and which includes structural tissues (leaves, fine roots and fruits, and for trees additionally coarse roots, sapwood and heart-wood) as well as two non-structural pools, labile and reserve. The canopy is divided into ten layers. The canopy scheme incorporates photosynthesis and canopy conductance separately for sunlit and shaded leaves for each canopy layer. Photosynthesis is represented using the model by Kull and Kruijt (1998), and extended to cover C4 plants (Friend et al., 2009)

Plants in QUINCY respond to soil N availability. This includes a response in leaf N content, which decreases if there is not enough N is available. Leaf nitrogen is divided into structural and photosynthetically active components. The photosynthesis scheme explicitly eonsiders accounts for the role of  $chl_{leaf}$ . This is done by calculating the light-harvesting limited rate of photosynthesis, taking into account the intrinsic quantum efficiency for  $CO_2$  uptake and the absorbed radiation of the canopy layers. The photosynthesis incorporates both Photosynthesis is calculated using the Kull and Kruijt (1998) model. According to this model, in the light-saturated and non-light-saturated part. The non-light-saturated part is dependent on  $J_{max,25}$ , which is the part of the leaf, photosynthesis is the minimum of electron transport rate-limited photosynthesis (determined by the maximum electron transport rate at 25 reference temperature. The parameter  $J_{max,25}$ ) and the carboxylation capacity-limited photosynthesis (determined by the maximum carboxylation capacity parameter  $V_{c(max),25}$ ). In the non-light-saturated part, photosynthesis is determined by the electron transport-rate-limited photosynthesis. Chlorophyll partly determines the depth of the light-saturated part is a dependent on both  $J_{max,25}$  and the maximum carboxylation rate at the 25 reference temperature  $(V_{c(max),25})$ , both co-limiting the photosynthetic rate. All rates are dependent on leaf nitrogen contentlayer in the leaf. Thus,

all the three photosynthetically active components of leaf nitrogen influence the photosynthesis calculation in OUINCY, as described by Friend et al. (2009), Zaehle and Friend (2010), and Thum et al. (2019).

205

210

220

225

230

235

The fast labile pool receives carbon via photosynthetic processes, and nitrogen via root uptake. In this study, phosphorus dynamics are not accounted for. Nitrogen uptake is a function of fine root biomass, soil inorganic nitrogen (ammonium and nitrate) and plant N demand. From the labile pool, nitrogen is either transferred to the reserve pool or allocated to tissue growth. C from the labile pool is used directly for maintenance respiration, which is prioritized over growth. Maintenance respiration is represented as a linear function of tissue N content for each pool. The photosynthesis model by Kull and Kruijt (1998) is extended to cover C4 plants (Friend et al., 2009).

The C:N ratios of leaves and fine roots respond dynamically to the balance of C and N in the labile pool. When there is shortage of N supply, the leaf C:N ratio increases and vice versa. The ratios are constrained to an empirically derived range based on the TRY database (Kattge et al., 2011).

, and the lower and upper boundaries are presented in Table S4. Soil carbon and nitrogen pools are modeled on the basis of the CENTURY soil model (Parton et al., 1993). There are five organic soil pools; metabolic, structural and woody litter 215 pools, a fast-overturning soil organic matter (SOM) pool and a slow-overturning SOM pool. There are also inorganic soil pools for ammonium (NH<sub>4</sub>) and nitrate (NO<sub>3</sub>). The and the soil profile is divided into 15 vertical soil layers, extending to a depth of 9.5 m with increasing depth when moving deeper into the ground. N uptake via biological nitrogen fixation (BNF) is included, both as an asymbiotic and symbiotic process (Meyerholt et al., 2016). Symbiotic N fixation is calculated taking into account the dynamic trade-off between C and N opportunity costs, based on Rastetter et al. (2001), Meyerholt et al. (2016) and Kern (2021).

The seasonal development of leaf biomass depends on the ability of the plant and LAI depend on the plant's ability to grow new tissuesand, given the availability of C and N, as well as the fractional allocation to plant organs. This fractional allocation is constrained by allometric relationships and the availability of nutrients and water. Meteorological conditions and soil moisture are used as phenological controls for LAI development, and it is assumed that plant growth is zero outside the growing season. Both the beginning and the end of the growing season, which determine the LAI seasonal cycle, depend partly on the PFT. For cold and temperate deciduous and herbaceous PFTs, the start of the season is described as a function of the accumulated growing degree days. The accumulated growing degree days are calculated from the beginning of the last dormancy period. In addition, for these PFTs, the end of the growing season is triggered when the weekly air temperature falls below a PFTspecific threshold. For PFTs of rain-deciduous phenology, the start of the season is triggered when the soil moisture stress factor exceeds the PFT-specific threshold values. For these PFTs and also for the warm herbaceous PFTs, the trigger for the end of the season is again the soil moisture stress factor. An additional condition for herbaceous PFTs to end their growing season is when the weekly carbon balance, i.e. the residual between GPP and maintenance respiration, becomes negative. The evergreen needle-leaved trees are assumed to be in a continuous growing season. A more detailed description of QUINCY is presented in Thum et al. (2019).

# 2.4.1 Original leaf nitrogen allocation in QUINCY

QUINCY allocates the total canopy nitrogen to canopy layers with exponentially decreasing N content towards the bottom of the canopy as in Niinemets et al. (1998). At the leaf level, nitrogen is partitioned into structural ( $f_{N,struct}$ ) and photosynthetic fractions at each canopy layer (Friend et al., 1997). The photosynthetic fractions are associated with chlorophyll ( $f_{N,chl}$ ), Rubisco ( $f_{N,rub}$ ), which is used directly to calculate  $V_{c(max)}$ , and electron transport ( $f_{N,et}$ ), which is used to calculate the maximum rate of electron transport ( $J_{max}$ ).

The fraction of leaf N in the structural compartment for each layer,  $f_{N,struct}$ , is calculated as a linear function of leaf N, as presented in Zaehle and Friend (2010):

$$f_{N,\text{struct}} = k_0^{\text{struct}} - k_1^{\text{struct}} * N_{\text{leaf}}$$
 (1)

where  $k_0^{\text{struct}}$  is the PFT-specific maximum fraction of structural leaf N, and  $k_1^{\text{struct}} = 7.14^3 \text{ (gN)}^{-1}$  is the slope of structural leaf N with respect to total N ( $N_{\text{leaf}}$ ) (Friend et al., 1997).

The fraction of leaf N in the chlorophyll compartment,  $f_{N,chl}$ , is calculated as an increasing function of cumulative LAI across the canopy (LAI<sub>cum</sub>) (Kull and Kruijt, 1998; Friend et al., 2009; Zaehle and Friend, 2010):

$$f_{N,chl} = \frac{k_0^{chl} - k_1^{chl} e^{-k_{fn}^{chl} * LAI_{cum}}}{a_s^{chl}}$$
(2)

where  $k_0^{\rm chl}$  and  $k_1^{\rm chl}$  are PFT-specific empirical parameters,  $k_{fn}^{\rm chl}$  is an empirical parameter describing the increasing  $f_{\rm N,chl}$  with canopy depth, and LAI<sub>cum</sub> is the cumulative LAI.  $a_n^{\rm chl} = 25.12~{\rm molmmol^{-1}}$  describes the molecular N content of chlorophyll (Evans, 1989). The  $k_0^{\rm chl}$  and  $k_1^{\rm chl}$  parameters are the same for trees and C3 grasslands, but different for C4 grasslands. The rest of the leaf N is divided between the  $f_{\rm N,rub}$  and the  $f_{\rm N,et}$  with a fixed ratio of 1.97 (Wullschleger, 1993).

#### 2.4.2 Alternative leaf N allocation

In the alternative leaf N allocation scheme,  $f_{N,rub}$  is calculated based on a function of leaf mass per area (LMA) as described by Onoda et al. (2017). The formulation using the QUINCY PFT-specific LMA values (Thum et al., 2019) is as follows:

$$f_{N,\text{rub}} = \frac{-21.1 * \log_{10}(\text{LMA}) + 57.5}{100}.$$
(3)

The fraction in electron transport,  $f_{N,et}$ , is derived from  $f_{N,rub}$  using the fixed ratio of 1.97.  $f_{N,chl}$  is then calculated as a function of  $f_{N,et}$ , based on the results by Evans and Clarke (2018) Evans and Clarke (2019):

260 
$$f_{N,chl} = \frac{37.3}{8.85 * 2.0} f_{N,et} e^{-k_n LAI_{cum}}$$
 (4)

where  $k_n = -0.11$  describes the increase in  $chl_{leaf}$  within the canopy depth. The  $f_{N,struct}$  is then calculated as the remaining part of the leaf N,  $(f_{N,struct} = 1 - f_{N,chl} - f_{N,rub})$ .

#### 2.5 Site description

270

275

280

285

290

295

# 2.4.3 QUINCY simulation setup

We conducted individual site-level QUINCY simulations, and the simulated sites were selected from two datasets. The first set was the Protocol for the Analysis of Land Surface Models (PALS) Land Surface Model Benchmarking Evaluation Project (PLUMBER2) (Ukkola et al., 2022). The second site set, GLOBAL, is based on the study by Caldararu et al. (2022).

PLUMBER2 (Abramowitz et al., 2024) was designed for serving in a model intercomparison project for land surface models, and provides CO<sub>2</sub> flux measurements and meteorological data. Of the available sites, we excluded sites with anomalous precipitation data (Abramowitz et al., 2024) and other issues, leaving 143 PLUMBER2 sites. The GLOBAL site set includes 279 sites representing all major climate zones and global biomes for the years 1989–2018 based on the CRU JRA dataset (Harris, 2020) for which RS chl<sub>leaf</sub> data were available and matched in land cover type. In total, the combined PLUMBER2 and GLOBAL analysis included 422 sites. The locations of the PLUMBER2 and GLOBAL sites are presented in Fig. S1, and the number of different PFTs in the site sets is listed in Table 1.

List of QUINCY PFTs and the corresponding number of sites in the PLUMBER2 and GLOBAIAsibraviation Long name Nr of sites, PLUMBER2 Nr of sites, GLOBAL Nr of sites, all BNE Boreal needle-leaved evergreen 20 50 70 TeNE Temperate needle-leaved evergreen 8 6 14 BNS Boreal needle-leaved deciduous 0 6 6 TeBE Temperate broad-leaved evergreen 4 4 8 TeBS Temperate broad-leaved deciduous 25 20 45 TrBR Tropical broad-leaved rain deciduous 2 2 4 TrBE Tropical broad-leaved evergreen 9 38 47 TeC C3 crops 21 0 21 TeH C3 grasslands 34 69 103 TrH C4 grasslands 20 84 104 all - 143 279 422-

We conducted individual site-level QUINCY simulations for the PLUMBER2 and GLOBAL sites. In QUINCY, C3 crops and C3 grasslands are grouped as one PFT, i.e. they are simulated with the same parametrization. The current version of QUINCY does not include management practices. Therefore, C3 crops do not differ from C3 grasslands in QUINCY simulations. Similarly, boreal and temperate needle-leaved evergreen forests are grouped into the same PFT. In this study, we labeled those as the needle-leaved evergreen sites with a mean annual temperature below 10 °C as boreal and the rest as temperate.

#### 2.5 Simulation setup

We ran all the simulations with active C and N cycles, i.e. the CN version of the model. Soil P availability was kept at a level that did not limit plant uptake or SOM soil organic matter decomposition. The model input fields included half-hourly meteorological data: shortwave (SW) SW and longwave radiation, air temperature, precipitation, surface air pressure, relative humidity and wind speed. In addition, atmospheric CO<sub>2</sub>, and N and P deposition rates are part of the input drivers. Model input parameters include PFT classification and various soil properties such as soil texture, bulk density, soil depth, rooting depth and inorganic soil P content. The specific leaf area (SLA), which is the inverse of LMA, is maintained as a PFT-specific constant. There is only one PFT associated with each site. The list of PFTs and the corresponding PFT abbreviations are presented in Table 1.

The For the PLUMBER2 sites, the meteorological fields were obtained from the PLUMBER2 dataset and (Ukkola et al., 2022). Depending on the PLUMBER2 site, meteorological data was available from 1992 to 2018 (Ukkola et al. (2022), Table S1).

For the GLOBAL sites, the meteorological data were obtained from the CRU JRA datasetas previously mentioned, and covered the years 1989–2018. Soil physical and chemical parameters (bulk density, rooting and soil depth and soil texture) were retrieved from the SoilGrid dataset (Hengl et al., 2017). Atmospheric CO<sub>2</sub> concentrations were retrieved from the Global Carbon Budget 2019 data (Friedlingstein et al., 2019), and the N and P deposition data are based on the dataset presented by Lamarque et al. (2010) and Lamarque et al. (2011).

For each site, we ran a 1000-year model spin-up in order to bring the soil and vegetation biogeochemical pools into quasi-equilibrium. Atmospheric-During the spin-up, atmospheric CO<sub>2</sub> concentrations were taken from a randomly selected year between 1901–1930, and meteorological concentration, N deposition and P deposition data were used by repeating the values from the period between 1901 and 1930. Meteorological data were taken from a random year of observed meteorological data. After spin-up, the simulations were conducted as transient simulations, starting from the year 1901. The transient simulation was carried out with meteorological data taken continued with data from a random year of observed meteorology. This was continued until the year when data from observed meteorology were available for until the respective years, start of the period for which observed meteorological data were available. For the PLUMBER2 sites, the start of the period was site-dependent, while for the GLOBAL sites, the meteorological data began in 1989. In the transient simulation, atmospheric CO<sub>2</sub> concentrations and N deposition were retrieved for the corresponding years from the data sources mentioned above.

In addition to the simulation with the default QUINCY setup for the PLUMBER2 and GLOBAL sites, we carried out four additional simulations for the PLUMBER2 sites to analyze how N limitation and changes in leaf nitrogen allocation affect the results. First, we performed an additional simulation with the QUINCY C-only setup (QUINCY  $C_{only}$ ), where only the C cycle was active but the leaf stoichiometry was described with a fixed parametrization. This was done in order to compare the effect of N limitation with the results of the default QUINCY CN-simulation. We then conducted a CN-simulation with the alternative leaf N allocation scheme, as described in Section 2.1.22.4.2. After that, we ran a CN-simulation using the default QUINCY settings, but modified the source code by multiplying the  $f_{N,chl}$  parameter by 1.3. This was done in order to see the effect of increasing fraction of leaf N allocated to  $chl_{leaf}$ . Finally, we carried out a simulation with the alternative leaf N allocation, but the  $f_{N,rub}$  was multiplied by 1.3, to represent a 30% increase in the Rubisco fraction, which leads to an increase in the  $chl_{leaf}$  fraction. The additional simulations with increased  $f_{N,chl}$  and  $f_{N,rub}$  were only performed for the temperate broad-leaved deciduous (TeBS) sites in the PLUMBER2 site set. The list of different simulations is presented in Table SHS5.

#### 2.5 Remote sensing data

300

310

320

325

#### 2.4.1 Remotely sensed chlleaf

We obtained chl<sub>leaf</sub> content from the global RS product by Croft et al. (2020). The RS chl<sub>leaf</sub> is derived from the ENVISAT MERIS full-resolution reflectance data with a two-stage radiative transfer model. The spatial resolution of the global RS chl<sub>leaf</sub> is 300 m, and the data are processed to a 7-day temporal resolution for the years 2003–2011. The chl<sub>leaf</sub> has been retrieved by first modeling the reflectance spectra at the leaf level using two separate models: the 4-Scale model (Chen and Leblanc, 1997) for forested and spatially clumped ecosystems, and the SAIL model (Verhoef, 1984) for cropland and grassland ecosystems.

The chl<sub>leaf</sub> has been then derived from the leaf reflectance spectra by using the PROSPECT leaf optical model (Jacquemoud and Baret, 1990).

A detailed description of the RS chl<sub>leaf</sub> product is presented in Croft et al. (2020).

In addition, we obtained chlorophyll content data based on the Sentinel-3 OLCI data (Reyes-Muñoz et al., 2022) for two needle-leaved sites for which we also had *in-situ* chl<sub>leaf</sub> measurements. The RS chl<sub>leaf</sub> product by Reyes-Muñoz et al. (2022) is generated by involving Gaussian process regression algorithms, and the training data for the algorithm consisted of simulated top of atmosphere radiance from coupled canopy radiative transfer model SCOPE and the atmospheric radiative transfer model 6SV. The aim was to further evaluate the magnitude and the seasonality of chl<sub>leaf</sub> for the needle-leaved evergreen boreal forests by using data from a different Earth observation instrument and also obtained with a different retrieval algorithm than with RS chl<sub>leaf</sub> by Croft et al. (2020).

#### 2.4.1 Remotely sensed LAI

335

345

350

355

We used the GEOV1 remotely-sensed leaf area index (LAI) product from the Copernicus Global Land Service (Baret et al., 2013)

, which is the same RS LAI product used to retrieve the RS chl<sub>leaf</sub> by Croft et al. (2020). GEOV1 LAI is derived from the SPOT-VGT satellite data and has a temporal resolution of ten days and a spatial resolution of 1. We used data for the years 2003–2011.

# 2.4.1 Post-processing of the RS data

As RS chl<sub>leaf</sub> depends in part on the assumed land cover (LC) type for each grid cell, it was important to ensure that the QUINCY chl<sub>leaf</sub> values for each site represented the same ecosystems as RS chl<sub>leaf</sub>. We compared the PFT values used in the OUINCY simulations with the LC values from a European Space Agency Climate Change initiative (ESA-CCI-LC) LC map (ESA, 2017), from which the LC types were also taken for the RS chl<sub>leaf</sub> retrieval modeling by Croft et al. (2020). A list of LC types is presented in Table S2, and the LCs associated with each PFT in our comparison are presented in Table S3. For each site, we first selected the site grid cell and the eight surrounding grid cells, i.e. the 3x3 cell area, from the ESA-CCI LC map. We then checked whether the QUINCY PFT matched the LC type for each of the grid cells, and added to a list those grid cells that had a matching land cover type to the QUINCY PFT. We then picked from the RS chl<sub>leaf</sub> grid data only those listed grid eells that had a matching land cover type, and calculated an area average RS chloar based on the listed cells. This area average was calculated separately for each time step. If there were no matching grid cells in the 3x3 surrounding cells, we extended the search to cover 5x5 surrounding cells, and looped through 25 grid cells. We then selected the matching cells from the 25 cells, and calculated the area average RS chl<sub>leaf</sub> for each time step. There were eight PLUMBER2 sites and 80 GLOBAL sites for which we did not find any matching grid cells, and these sites were excluded from the analysis. We only used the top-of-canopy ehl<sub>leaf</sub> values from QUINCY to ensure that the values were consistent with the RS-based values. In addition, the RS chl<sub>leaf</sub> for the needle-leaved sites was multiplied by  $\frac{\pi}{2}$ . This was done to account for the half-hemispherical needle geometry in the remote sensing retrieval (Stenberg et al., 1995).

The RS LAI data were only retrieved using the one grid cell where the site was located, i.e. the PFT classification of a site did not affect the RS LAI post-processing. If no data were available in that particular grid cell, we extended the area to cover ±0.01latitude and longitude degrees and used the average of the whole extended area.

#### 2.5 *In-situ* observations

380

385

390

#### 2.4.1 Eddy covariance flux observations

Ground station GPP observations were available for the PLUMBER2 sites, and the data were taken from the eddy covariance flux tower dataset provided by Ukkola et al. (2022). The dataset includes flux tower data from three data releases: FLUXNET2015 (Pastorello et al., 2020), La Thuile (FLUXNET, 2024), and OzFlux (Isaac et al., 2017). The flux data were gap-filled using statistical methods depending on the length of the gap. The short gaps up to four hours were gap-filled using linear interpolation methods. Gaps that were longer than four hours were gap-filled with linear regression against the incoming SW radiation, air temperature and humidity, or only against the SW radiation if the other two variables were missing. Depending on the site, the flux time series ranged from one to 20 years, between the years 1992 and 2018 (See Ukkola et al. (2022) Table S1). Data from all years were used, and therefore, the GPP time series are not from the same time interval as RS chlacat.

# 2.4.1 chl<sub>leaf</sub> and leaf C:N in-situ measurements

To investigate the chl<sub>leaf</sub> magnitude and seasonal cycle for the evergreen needle-leaved forests, we performed an additional comparison for RS and QUINCY output with *in-situ* observations for two sites: Sodankylä site (FI-Sod) in Finland (67.4 N, 26.6) (Thum et al., 2007) and Niwot Ridge (US-NR1) in the United States (40.033 N, -105.546E) (Bowling and Logan, 2019). Both sites are characterized as needle-leaved forest sites with strong seasonal cycle and harsh winters. FI-Sod is classified as boreal forest, and US-NR1 as subalpine, and is located in a mountainous terrain. The sites were selected as both sites had a time series of chl<sub>leaf</sub> observations, and there were also radiation *in-situ* observations available at FI-Sod.

To determine the chlorophyll content of the crowns in Sodankylä, there were taken in total 160 biweekly needle samples from the south and north faces of crowns of three mature Scots pine (*Pinus sylvestris*) trees during 31.3–30.9.2015. Needle samples were taken separately for one- and three-year-old shoots of branches that were cut with clippers from the upper part of the crowns. Each sample consisted of four pairs of needles that were immediately immersed in liquid nitrogen in a portable dewar (CX-100, Taylor Wharton International LLC, Minnetonka, MN), and subsequently stored at -80 until extraction. Pigments were analysed by using a method following Wellburn (1994) with dimethyl sulfoxide (VWR Chemicals, 23500.322) as solvent. Frozen needle samples (75—100 ) were first homogenized for 2 minutes at 30 , using a bead mill (TissueLyser II Qiagen, Germany), stainless steel beads (4 mm), and microtubules (2 ). Subsequently, 1.8 of dimethyl sulfoxide was added to the homogenate and resuspended again at 30 for one minute. Pigments were extracted in oven at 40 for 4. The extracts were then centrifuged at 25000 g for five minutes. Light absorption was measured at 649.1, 665.1, and 480.0, with a spectrophotometer (Shimadzu UV-2401 PC), and subsequently used in the estimation of chl A, chl B, and total carotenoids (Wellburn, 1994). The Sodankylä chl<sub>leaf</sub> measurements represent both chlorophyll A and B (chl<sub>a+b</sub>).

The US-NR1 pigment measurements represent two tree species: lodgepole pine (*Pinus contorta*) and Engelmann spruce (Picea engelmannii). The measurements were collected from tree branches and the pigments were extracted in solvent, and then analyzed by liquid chromatography (Bowling and Logan, 2019). We calculated the daily average value of chlicat over measurements from several trees, and filtered out the days when fewer than three samples were available. For FI-Sod, we also had in-situ measurement data for the fraction of absorbed photosynthetic radiation (fAPAR) for the years 2021–2024 which were measured with the PQS1 instrument with factory calibration (Knorr et al., 2025). We excluded those days from in-situ fAPAR measurements for which the 2021–2024 daily mean photosynthetically active radiation (PAR) below canopy was less than one. This was done in order to filter out measurement data that might not be representative due to reduced sun light and potential snow cover. We also used in-situ observations from the TRY database (Kattge et al., 2011) to compare the in-situ leaf C:N ratios with our model-derived values. The leaf C:N observations were retrieved from the TRY database for two sites: the boreal needle-leaved forest station Hyytiälä in Finland (FI-Hyy, 61.8N, 24.3E) and the deciduous forest site, Morgan Monroe State Forest site in the US (US-MMS, 39.3N, -86.4E). The FI-Hyy measurements are sampled from Scots pine tree. US-MMS is a secondary successional broad-leaved forest, and the leaf C:N measurements cover various different deciduous trees: sugar maple (acer saccharum), American beech (fagus grandifolia), American elm (Ulmus americana), Northern red oak (Quercus rubra), and other deciduous species. The sites were selected based on consistent measurement time with the QUINCY simulations, and to expand the geographical gradient of in-situ measurements, and also to include an example of a TeBS site.

# 2.5 Feature importance analysis

395

400

405

420

425

The impact of different environmental drivers on the simulated and RS chl<sub>leaf</sub> magnitude was examined using the permutation feature importance algorithm, based on random forest (RF) regression fitting (Breiman, 2001). RF is a regression tree-based machine learning method that is able to capture non-linear correlations. Permutation importance indicates the contribution of an individual input variable to the statistical performance of a model. In other words, permutation importance can be used to investigate the influence of an environmental driver on a target variable, which in our case is chl<sub>leaf</sub>. In addition, we analyzed the importance of each selected environmental variable via the SHAP (SHapley Additive exPlanations, (Lundberg and Lee, 2017)) values. We used the SciKit Learn Python3 package for both RF and permutation importance (Pedregosa et al., 2011), and the *shap* Python library by Lundberg and Lee (2017) (https://github.com/shap/shap; last access June 23, 2025) to compute the SHAP values.

The target data for the RF models were either QUINCY chl<sub>leaf</sub> or RS chl<sub>leaf</sub>. We trained 20-22 separate RF models. Of the 2022, the first nine ten RFs were dedicated to monthly QUINCY chl<sub>leaf</sub> and each individual PFT from PLUMBER2 and GLOBAL sites. In addition, we trained one RF model with monthly data from all of the sites and QUINCY chl<sub>leaf</sub>, using both PLUMBER2 and GLOBAL sites. The remaining RF models were used for monthly RS chl<sub>leaf</sub> and individual PFTs, and one model with data from all of the sites.

The input data consisted of monthly means of air temperature and PAR, and annual sums of precipitation and N deposition, and annual means of Standardized Precipitation Evapotranspiration Index (SPEI) at each of the sites. The input variables for

the RF models were selected from the available environmental data that showed the least correlation between each other. Air temperature, precipitation and N deposition were those used as input in the QUINCY simulations. The SPEI data were retrieved from the global drought monitoring dataset by Vicente-Serrano et al. (2023). We used the SPEI with a two-week time scale (SPEI 0.5 months), which was then averaged as monthly mean data. The spatial resolution of the SPEI dataset was  $0.5^{\circ} \times 0.5^{\circ}$ , and we chose the same time steps as in the QUINCY data. The PAR radiation was taken from the QUINCY output, and it is converted from SW radiation with the model (Howell et al., 1983).

The random forest hyperparameters were set to default values, but the maximum number of features per node was set to three. A recommended value for the maximum number of features per node in RF regression is one-third of the input features (Hastie et al., 2009), but here we used a slightly higher value in order to maintain representative subset sizes. After training the RF-models

First, we tested the performance of RF models by splitting the data using the *train\_test\_split* function in SciKit Learn. We used 75 % of the data for preliminary training and 25 % for preliminary testing. The coefficient of determination (R<sup>2</sup>) scores for the preliminary training and preliminary testing phases are reported in Table S6. Next, we used all the data (i.e., the preliminary training and preliminary testing data) for the final training of the models.

After the final RF model training, we calculated the corresponding permutation feature importance values for each model. The permutation feature importance algorithm was used with 30 repeats (n\_repeats = 30) and with a fixed random state. Finally, the SHAP values were calculated using data averaged over three months. The higher positive SHAP values indicate a stronger, increasing effect on chl<sub>leaf</sub>, and the lower negative SHAP values indicate a decreasing effect on chl<sub>leaf</sub> compared to the average.

## 445 **2.6 Data-analysis**

430

435

In this study, the QUINCY chl<sub>leaf</sub> is the top-of-canopy chl<sub>leaf</sub>, as mentioned in Section 2.4.32.2.3. For the PLUMBER2 sites, we used all the available years from the QUINCY simulations, as well as from RS and eddy covariance observations. For the GLOBAL sites, we used QUINCY simulation data for the years in which RS chl<sub>leaf</sub> data was available for each site.

We calculated the PFT mean chl, LAI 90th percentile for GLOBAL and PLUMBER2 sites for both QUINCY and RS. In addition, we calculated the PFT mean annual GPP for GLOBAL and PLUMBER2 sites for QUINCY, but only the PFT mean for the GPP ground observations on the PLUMBER2 sites, as no GPP ground station measurements were available for the GLOBAL (artificial) sites. We used the 90th percentile of LAI instead of the mean values. This was done to reduce the effect of seasonal variation differences in seasonal amplitude and timing variation between QUINCY and RS and to focus on LAI values during the growing season. We calculated the Pearson correlation coefficients (r) between QUINCY and RS site-level mean chl<sub>leaf</sub>, LAI 90th percentile and GPP annual sum values, and the statistical significance of the correlation using Student's t-test, with a threshold value of 5 % for the statistical significance.

We analyzed the seasonal cycle of chl<sub>leaf</sub>, LAI and GPP for one specific site, Hainich in Germany (DE-Hai, 51.08°N, 10.45°E). The Hainich site is located in the middle of a beech forest, and is characterized as a deciduous broad-leaved forest (TeBS). We also studied the seasonal cycle over all PFTs for the Northern Hemisphere (NH) sites by comparing the

460 monthly PFT averages of QUINCY chl<sub>leaf</sub> and RS chl<sub>leaf</sub>. Tropical broad-leaved evergreen (TrBE) sites did not show detectable seasonality in either QUINCY or RS, and therefore these sites have been omitted from the seasonality analysis. In addition, we calculated the average values over April, May, October and November for the PLUMBER2 TeBS NH sites for the QUINCY results and observations, to study the differences in seasonal development.

We analyzed the seasonal cycle of chlleaf and LAI for the PLUMBER2 and GLOBAL Northern Hemisphere (NH) sites separately for different PFTs. In addition, the analysis of the PLUMBER2 sites included GPP. First, we calculated the averaged 465 seasonal cycle over years for each site and variable. Then, using these averaged seasonal cycles, we calculated the mean seasonal cycle per PFT across sites and the standard deviation between sites for each day of year (DOY). This was done for QUINCY simulated values and for RS and eddy covariance CO<sub>2</sub> observations. Using the PFT-averaged seasonal cycles, we calculated the Pearson correlation (r) and root mean squared error (RMSE) between OUINCY and the observations. For the NH PLUMBER2 TeBS sites, we estimated the start of season (SOS), the end of season (EOS) and the length of season 470 (LOS) based on the PFT-averaged chl<sub>leaf</sub>, LAI and GPP. We calculated the seasonal metrics using the method as described by Thum et al. (2025). The SOS and EOS values from the PFT-averaged GPP were calculated using the first and last pass of the threshold value. The threshold was set at 30 % of the 90th percentile value of the PFT-averaged mean seasonal cycle of GPP. For LAI and chl<sub>leaf</sub>, the threshold was determined using the difference between the summer and winter values. Winter values were calculated using the mean values from January and February, and summer values were calculated using 475 the mean values from June and July. The threshold was then set to 20 % of the difference, added to the winter mean, (i.e.,  $y_{thres} = x_{winter} + 0.2*(x_{summer} - x_{winter})$ ). The earliest DOY for SOS was set to 50. LOS was calculated as the difference between EOS and SOS.

We calculated the residuals between the QUINCY chl<sub>leaf</sub> mean and RS chl<sub>leaf</sub> for each site, and compared these to the QUINCY leaf C:N ratios. Leaf C:N can be considered as an indicator of availability for plants. The aim was to examine whether the under- or overestimation of QUINCY chl<sub>leaf</sub> was related to nitrogen limitation in the model. The comparison was done for BNE, TeH and TeBS. These PFTs were assumed to represent different vegetation types: BNE represents evergreen forests, TeH grasses and TeBS deciduous forests. In addition, we calculated the mean chl<sub>leaf</sub> interannual variability (IAV) for the PLUMBER2 and GLOBAL sites. We first calculated the standard deviation of the annual mean chl<sub>leaf</sub> for each site, and then the average of the standard deviations at the PFT level and over all sites.

485

490

We analyzed the seasonal cycle of chl<sub>leaf</sub> for two evergreen needle-leaved PLUMBER2 sites, FI-Sod and US-NR1 (see Section 2.3.2), by comparing the QUINCY simulations, *in-situ* observations and remote sensing observations. We calculated the averaged seasonal cycles over years for QUINCY and for remote sensing chl<sub>leaf</sub> and compared them with *in-situ* observations. Furthermore, we analyzed the seasonal cycles of LAI, fAPAR and GPP for the FI-Sod site and compared the QUINCY simulated values to the observations. We also compared briefly the simulated mean annual averaged leaf C:N values to *in-situ* observations for two PLUMBER2 sites, FI-Hyy and US-MMS.

## 3 Results

505

510

515

520

# 3.1 Evaluation of simulated chl<sub>leaf</sub>, LAI and GPP against observations

#### 3.1.1 Yearly values

At the PFT level, QUINCY estimates of the mean annual chl<sub>leaf</sub> and LAI agree relatively well with the RS-derived chl<sub>leaf</sub> and LAI values (Figs. 1, S2, S3 and Tables \$4\$7 and \$5\$.8) for all PLUMBER2 sites, with correlations of r = 0.61 for chl<sub>leaf</sub> and r = 0.51 for LAI (Table \$4\$7.) QUINCY does overestimate both chl<sub>leaf</sub> and LAI for TeBE and TrBR sites, with TeNE and TeC also overestimated for LAI on a mean PFT scale. Despite the variability in simulated chl<sub>leaf</sub> and LAI values in comparison to RS-derived values, the overall simulated GPP for all PLUMBER2 sites correlates well between QUINCY estimates and eddy-covariance data (r = 0.71; Table \$4\$7 and Figure \$4\$).

As expected, the within PFT variability between sites reveals greater scatter, the nature of which differs for chl<sub>leaf</sub> and LAI (Figs. S2, S3). For chl<sub>leaf</sub> in all cases apart from TeBS, TrBE and TrH, there is a lack of variation in the QUINCY chl<sub>leaf</sub>, which present more constant values and smaller dynamic range compared to RS chl<sub>leaf</sub> values (Fig. S2 and Tables \$4\$7, \$5\$8). This is particularly pronounced for TeC and TeH sites, which gives give a range of 10–17 μg cm<sup>-2</sup> for TeC and 4-17 μg cm<sup>-2</sup> for TeH, for QUINCY and a range of 13–46 μg cm<sup>-2</sup> and 2–47 μg cm<sup>-2</sup> for RS, respectively. The site-level LAI estimates by construst contrast generally present a larger dynamic range (with the exception of TeBs, TeNE, TeBE and TrBE). The TrH in particular show a large overestimation in QUINCY LAI compared to RS LAI at higher LAI values (LAI > 2.5) (Figure Fig. S3). The site-level GPP results show a good correlation between QUINCY estimates and eddy-covariance observations across PFTs. Whilst the correlation is generally along the 1:1 line, in 58 % of the PLUMBER2 sites, QUINCY underestimates the GPP on average by about 400 gC m<sup>-2</sup> yr<sup>-1</sup>. The majority of these underestimations are for BNE and TeBS forests. The QUINCY overestimation of GPP is mainly for crops and grasslands, with an average overestimation of 384 gC m<sup>-2</sup> yr<sup>-1</sup> across 42 % of the PLUMBER2 sites. For the PLUMBER2 sites, the slight LAI overestimation of the TrH sites does not seem to lead to an overestimation of the mean GPP, but the QUINCY PFT mean GPP (756 gC m<sup>-2</sup> yr<sup>-1</sup>) is lower than the PFT mean of the observations (902 gC m<sup>-2</sup> yr<sup>-1</sup>). Due to very high LAI values for the GLOBAL TrH sites, the QUINCY mean GPP for the GLOBAL TrH sites was 1461 gC m<sup>-2</sup> yr<sup>-1</sup> (not shown), and QUINCY chl<sub>leaf</sub> mean was 50.2 μg cm<sup>-2</sup>.

The QUINCY over- or underestimation in chl<sub>leaf</sub> did not have a strong, detectable geographical pattern when assessed together and separately for all PFTs. The residual chl<sub>leaf</sub>, i.e. the difference between the mean QUINCY and RS values, is shown in Fig. S5 on a map showing the geographical location of each site. For the C3 grassland sites, the QUINCY mean chl<sub>leaf</sub> was rather small compared to the RS chl<sub>leaf</sub>. When analyzing the residuals for the C3 grasslands, the northernmost sites seem to have less negative residuals in magnitude than for the sites around latitudes 30–60°N. This was also the case when the relative residual was analyzed (not shown). The greater QUINCY underestimation of chl<sub>leaf</sub> for the warmer, southern C3 grassland sites is not related to the GPP underestimation. Interestingly, for the GLOBAL C3 grassland sites the LAI over/underestimation shows an opposite pattern to QUINCY chl<sub>leaf</sub>: the northern sites show more negative LAI residual, and

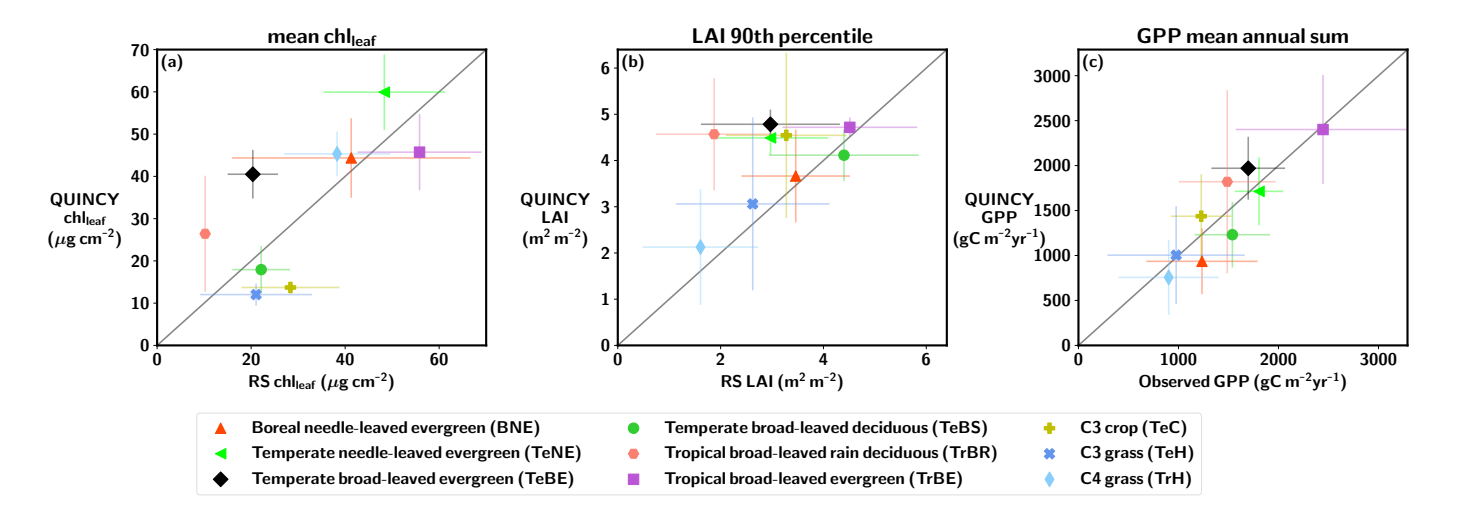


**Figure 1.** The PFT mean (a) chl<sub>leaf</sub>, (b) LAI and (c) GPP for the PLUMBER2 sites. The standard deviation is represented by whisker lines. A 1:1 line is marked with a gray line.

sites around latitudes 30–60°N mostly QUINCY overestimation of LAI (not shown), which could be due to the fact that RS chl<sub>leaf</sub> is calculated using RS LAI.

The mean IAV of RS chl<sub>leaf</sub> over all PFTs is  $4.11\pm3.18~\mu g~cm^{-2}$ , which is much higher than the corresponding value for QUINCY ( $1.35\pm1.52~\mu g~cm^{-2}$ ). The RS chl<sub>leaf</sub> IAV is higher for all other PFTs except for TrH, where the QUINCY chl<sub>leaf</sub> IAV was  $3.39\pm2.04~\mu g~cm^{-2}$ , and the RS chl<sub>leaf</sub> IAV was  $3.37\pm2.35~\mu g~cm^{-2}$ . The largest differences in IAVs between RS and QUINCY were seen for the evergreen sites. For example, the RS chl<sub>leaf</sub> IAV for the BNE sites is  $5.95\pm3.51$ , and the QUINCY chl<sub>leaf</sub> IAV is  $0.5\pm0.4~\mu g~cm^{-2}$ .

# 3.1.2 Seasonal cycle

525

530

535

540

The most visible difference between QUINCY and RS chl<sub>leaf</sub> seasonality can be observed for the boreal and temperate evergreen sites (Fig. 2a,b,e,d): QUINCY shows very little variation across seasons, while the RS chl<sub>leaf</sub> indicates more variation throughout the year.

For the BNS and TeBS sites (Fig. 2b,e), QUINCY does contain a seasonal pattern. However, the seasonal cycle in QUINCY is delayed in the fall compared to RS for BNS and TeBS. QUINCY produces the highest monthly mean chl<sub>leaf</sub> for the summer, but September is also at the same level. The annual cycle of chl<sub>leaf</sub> at the Hainich site (Fig. 3) is very similar when comparing QUINCY and RS. However, the start of the growing season is delayed in QUINCY, and the simulated LAI increases approximately 20 days later in spring compared to the RS LAI. The delay is even more pronounced for chl<sub>leaf</sub>, as the simulated chl<sub>leaf</sub> increases approximately 40 days later compared to the RS chl<sub>leaf</sub>. Similarly, the end of the growing season is delayed in QUINCY. While the RS LAI shows a decrease throughout the autumn season, QUINCY LAI remains at a high value until day of year (DOY) 280, which corresponds to mid-October. However, despite the fact that QUINCY chl<sub>leaf</sub> and LAI remain

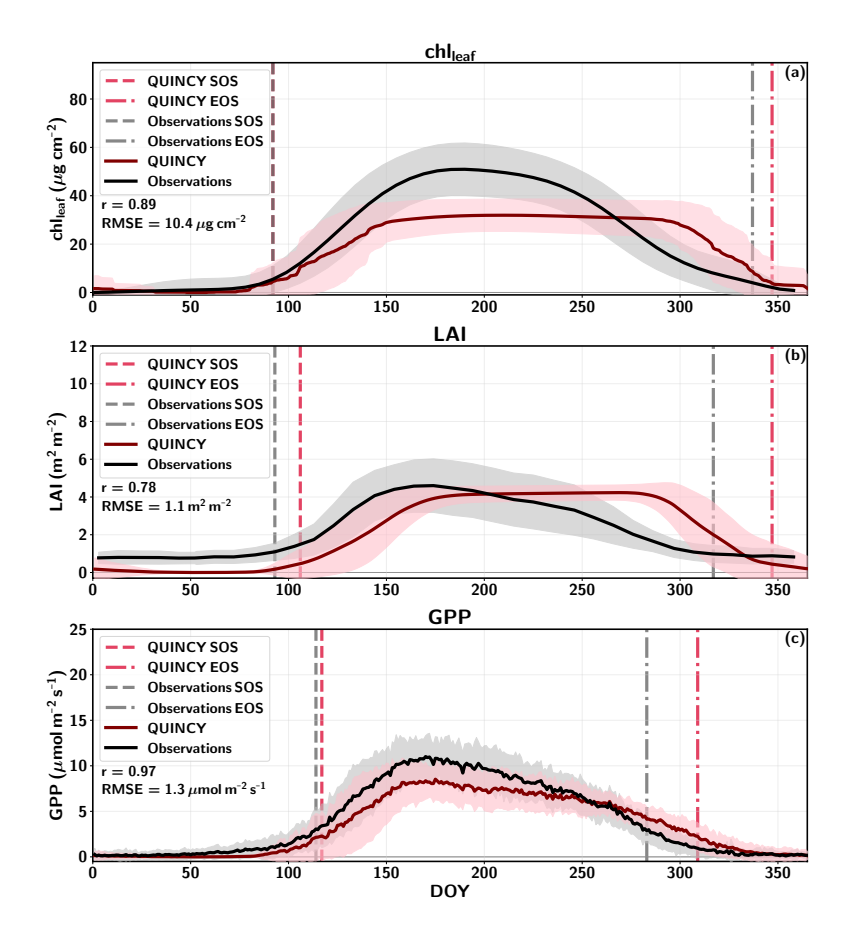


Figure 2. The average annual cycle of (a) chl<sub>leaf</sub>, (b) LAI, and (c) GPP for the PLUMBER2 TeBS NH sites, as a function of the day of year (DOY). The shaded regions represent the standard deviation between sites. The start of season (SOS) and end of season (EOS) are marked with red (QUINCY) and grey (observations) vertical lines. The Pearson correlation (r) and root mean squared error (RMSE) are marked for each variable.

higher, their winter level is reached almost at the same time as in the Hainich observations, because the senescence occurs more rapidly in QUINCY than in the observations. Therefore, the overestimation in GPP is not as pronounced. Figure 3e shows that the GPP between DOY 90–150 for QUINCY is remarkably lower than in the observations at DE-Hai. The spring development of GPP is delayed. Although this is partially compensated for by the delayed end of the season where the QUINCY GPP is higher than the observed GPP after DOY 275, the spring difference makes a larger contribution to the annual GPP difference of 258 gC m<sup>-2</sup> yr<sup>-1</sup>. The mean annual QUINCY GPP is 1339±125 gC m<sup>-2</sup> yr<sup>-1</sup>, and the observed FLUXNET GPP is 1597±99 gC m<sup>-2</sup> yr<sup>-1</sup> between years the 2003–2011 (excluding 2005). In addition, although the simulated LAI remains at the summer level until DOY ~280, the simulated GPP decreases due to the environmental conditions.

545

550

The annual cycle of chl<sub>leaf</sub> for the PLUMBER2 NH TeBS sites (Fig. 2) is similar when comparing QUINCY and RS. However, the start of the growing season is delayed in QUINCY. The SOS, EOS and LOS values for the PFT-averaged

PLUMBER2 NH TeBS sites are presented in Table S9. The QUINCY SOS for LAI is approximately 13 days later in spring compared to the RS LAI. Similarly, the end of the growing season is delayed in QUINCY, and the EOS of QUINCY chl<sub>leaf</sub> occurs approximately 10 days later than in RS chl<sub>leaf</sub>. While the RS LAI shows a decrease throughout the autumn season, QUINCY LAI remains at a high value until day of year (DOY) 280, which corresponds to mid-October. The EOS for QUINCY LAI is approximately 30 days later than for RS LAI.

555

560

565

570

585

Figure 2c shows that the GPP between DOY 90–150 for QUINCY is slightly lower than in the observations. The spring development of GPP is slower in QUINCY than in the observations, though the QUINCY SOS of GPP occurs almost at the same time as in the measurements. Although the simulated LAI remains at the summer level until DOY ~280, the simulated GPP decreases due to the environmental conditions in autumn. However, the delay in autumn LAI senescence is reflected in the QUINCY GPP EOS, which is approximately 26 days later than for the GPP observations. The delay in the QUINCY spring GPP is compensated partly for by the delayed end of the season where the QUINCY GPP is higher than the observed GPP after DOY 275. The mean GPP 3-month sum for the PLUMBER2 NH TeBS sites for spring (March, April and May, MAM) is 289 gC m<sup>-2</sup> for the observations, while for QUINCY, the value is 196 gC m<sup>-2</sup>. The corresponding 3-month sum values for autumn (September, October, November, SQN) for observations is 256 gC m<sup>-2</sup>, and 351 gC m<sup>-2</sup> for QUINCY.

Figures S6 and S7 show the PFT-mean seasonal cycles of  $chl_{leaf}$  and LAI for the PLUMBER2 and GLOBAL NH sites, and S8 for GPP for the PLUMBER2 NH sites. The most visible difference between QUINCY and RS  $chl_{leaf}$  and LAI seasonality can be observed for the boreal and temperate evergreen sites (Fig. S6 a,c,f and Fig. S7a,c,f): QUINCY shows very little variation across seasons, while the RS indicates more variation throughout the year with a clear seasonal cycle. Nevertheless, the QUINCY GPP for these PFTs (Fig. S8a,b,e) shows a similar annual cycle as the eddy covariance observations, and the correlation r for the evergreen needle-leaved sites is high (r > 0.95). For the BNS sites (Fig. S6b and Fig. S7b), the biases in seasonal cycle were similar to the TeBS results (Fig. S6d and Fig. S7d).

QUINCY chl<sub>leaf</sub> for TeH and TeC sites show a delay in spring compared to RS chl<sub>leaf</sub>, but this was not observed for QUINCY LAI. In autumn, the decrease in QUINCY chl<sub>leaf</sub> and LAI occur later than in RS. For the TrH sites (Fig. 2iS6j), the seasonal cycle of QUINCY chl<sub>leaf</sub> and LAI differ from the observed seasonal cycle. The lowest PFT mean chl<sub>leaf</sub> for QUINCY is in April, suggesting that the phenological cycle for these sites needs further tuning in QUINCY(DOY~100). Of the 47 TrH sites in the NH, 74 % of the sites had a higher QUINCY winter (December, January, February, DJF) chl<sub>leaf</sub> average compared to the QUINCY spring (March, April, May, MAM) chl<sub>leaf</sub> mean. Furthermore, 55 % of the TrH NH sites were such that the QUINCY DJF means of both chl<sub>leaf</sub> and LAI were higher than the QUINCY MAM means. This suggests that the lower QUINCY spring chl<sub>leaf</sub> compared rest of the year for TrH sites could be due to a drought, which reduces LAI. RS chl<sub>leaf</sub> shows (Fig. S6j) the largest TrH averages for summer (JJA) and September, and a fairly clear seasonal cycle.

The late onset of chl<sub>leaf</sub>, LAI and GPP, and also the delayed decline in the fall, is distinguishable for the majority of the PLUMBER2 temperate deciduous broad-leaved sites (TeBS, Fig. S6). The April and May chl<sub>leaf</sub> values are mostly underestimated by QUINCY for chl<sub>leaf</sub>, LAI and GPP, while the October and November values are overestimated. For other PFTs, the monthly QUINCY chl<sub>leaf</sub> values do not show as clear spring underestimation and fall overestimation relative to RS as TeBS.

# Sodankylä (FI-Sod)

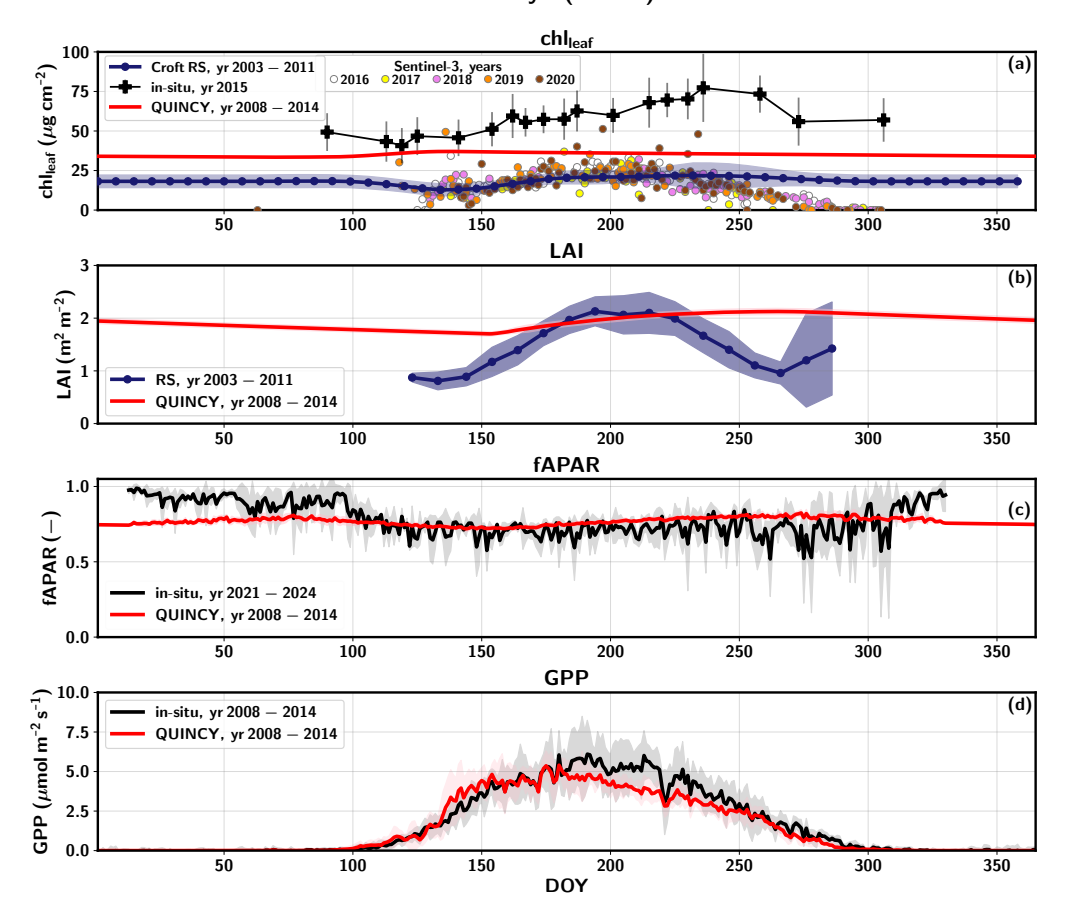


**Figure 3.** Seasonal cycle of daily means for FI-Sod (a) chl<sub>leaf</sub>, (b) LAI, (c) fAPAR and (d) GPP for QUINCY, remote sensing (RS) and *in-situ* measurements. The standard deviation for some of the data series is visualized as a shaded area. The Sentinel-3 chl<sub>leaf</sub> values for different years are shown with different colors (2016=white, 2017=yellow, 2018=pink, 2019=orange, 2020=brown).

The mean IAV of RS  $chl_{leaf}$  over all PFTs is  $4.11\pm3.18$ , which is much higher than the corresponding value for QUINCY (1.35 $\pm1.52$ ). The RS  $chl_{leaf}$  IAV is higher for all other PFTs except for TrH, where the QUINCY  $chl_{leaf}$  IAV was  $3.39\pm2.04$ , and the RS  $chl_{leaf}$  IAV was  $3.37\pm2.35$ . The largest differences in IAVs between RS and QUINCY were seen for the evergreen sites. For example, the RS  $chl_{leaf}$  IAV for the BNE sites is  $5.95\pm3.51$ , and the QUINCY  $chl_{leaf}$  IAV is  $0.5\pm0.4$ .

# 3.1.3 *In-situ* comparison of chl<sub>leaf</sub> for two needle-leaved forests

590

The seasonal cycle of chl<sub>leaf</sub>, LAI, fAPAR and GPP for Sodankylä is shown in Fig. 43, and the chl<sub>leaf</sub> values of the US-NR1 site are presented in Fig. 87S9. The mean annual and seasonal chl<sub>leaf</sub> and GPP values are presented in Table 86S10.

Figure 43a highlights that the QUINCY chl<sub>leaf</sub> values are in a range comparable to the *in-situ* observations for FI-Sod, but the QUINCY mean (Table \$6\$10) is lower than the annual mean of the *in-situ* measurements. On the contrary, the RS chl<sub>leaf</sub> by Croft et al. (2020) shows much lower values. In addition, the mean of the Sentinel-3 RS chl<sub>leaf</sub> is also lower than the *in-situ* or QUINCY chl<sub>leaf</sub> but close to the mean RS chl<sub>leaf</sub> by Croft et al. (2020).

600

605

615

620

The RS LAI in Fig. 43b shows a clear seasonal pattern for FI-Sod, which has a small effect on the RS chl<sub>leaf</sub>. The summer (JJA) average RS chl<sub>leaf</sub> is approximately 10% higher than the winter (DJF) average, which is a relatively small difference compared to the interannual variability ( $\sim 4\mu g \, \mathrm{cm}^{-2}$ ). In addition, the late spring RS chl<sub>leaf</sub> between DOY 100–151 show lower values than winter or summer. The late spring RS chl<sub>leaf</sub> averages  $14.6 \, \mu g \, \mathrm{cm}^{-2}$ , approximately 27% less than the JJA average. Similar spring decreases in RS chl<sub>leaf</sub> were also observed for other BNE sites. The Sentinel-3 chl<sub>leaf</sub> peaks in midsummer, and also shows a clear seasonal pattern. The *in-situ* chl<sub>leaf</sub> is slightly higher in late summer (DOY 200–240) compared to spring and fall.

QUINCY LAI shows a small seasonal variation, which is reflected in the simulated chl<sub>leaf</sub>. The winter (December–February, DJF) QUINCY average is slightly lower than the summer (June–August, JJA) QUINCY average chl<sub>leaf</sub>. The *in-situ* fAPAR values are in agreement with the simulations during most of the year, but show a stronger seasonal variation than the QUINCY fAPAR (Fig. 43c), with higher values during winter.

QUINCY GPP is in line with the observations until DOY 175, but then decreases until the end of the season (Fig. 43d). However, the difference in annual GPP is not large, and annual QUINCY GPP is on average approximately 9 % lower than the *in-situ* GPP. The difference between observed and simulated GPP after DOY 175 could be due to missing late fall chl<sub>leaf</sub> development or due to too strong response to a drought.

The mean *in-situ* chl<sub>leaf</sub> for the US-NR1 site was close to the QUINCY chl<sub>leaf</sub> mean (Fig. \$759 and \$6Table \$10). The minimum value of individual tree samples was  $26.8 \ \mu g \ cm^{-2}$  and the maximum was  $60.8 \ \mu g \ cm^{-2}$ , i.e. there was variation between individual samples that is partially minimized by the averaging. The *in-situ* observations show a slight increase during spring, but the variation is large due to the small number of samples. The mean *in-situ* chl<sub>leaf</sub> for DOY 1–150 is  $37.1\pm6.1 \ \mu g \ cm^{-2}$ , while the mean for summertime (JJA) is  $43.2\pm2.3 \ \mu g \ cm^{-2}$ . The summer (JJA) QUINCY chl<sub>leaf</sub> was close to the annual mean, i.e. there was no pronounced seasonal cycle. The RS chl<sub>leaf</sub> annual mean by Croft et al. (2020) was lower than the annual mean chl<sub>leaf</sub> of *in-situ* measurements or QUINCY. Interestingly, the RS chl<sub>leaf</sub> shows a lower JJA mean than the annual mean. Similarly to the FI-Sod RS chl<sub>leaf</sub>, there is a decrease in the spring chl<sub>leaf</sub> after DOY 100, and the decrease is more pronounced than for Sodankylä. The minimum value ( $\sim$ 16  $\mu$ g cm<sup>-2</sup>) of RS chl<sub>leaf</sub> averaged annual cycle appears around DOY 155, with an increase after that. For the Sentinel-3 chl<sub>leaf</sub>, the mean chl<sub>leaf</sub> was close to the QUINCY values, although the numerical range was much wider. The JJA mean for Sentinel-3 is close to the *in-situ* observations, and approximately 32 % higher than the QUINCY JJA chl<sub>leaf</sub>. The annual QUINCY GPP was 45 % lower than the observed GPP. In addition, the QUINCY JJA LAI (not shown) was  $2.2\pm0.1 \ m^2 \ m^{-2}$ , and was lower than the RS JJA LAI ( $2.5\pm0.2 \ m^2 \ m^{-2}$ , which may partially explain the underestimation of GPP. Bowling et al. (2018) report that the observed in-situ LAI at the site is 3.8–4.2  $m^2 \ m^{-2}$ .

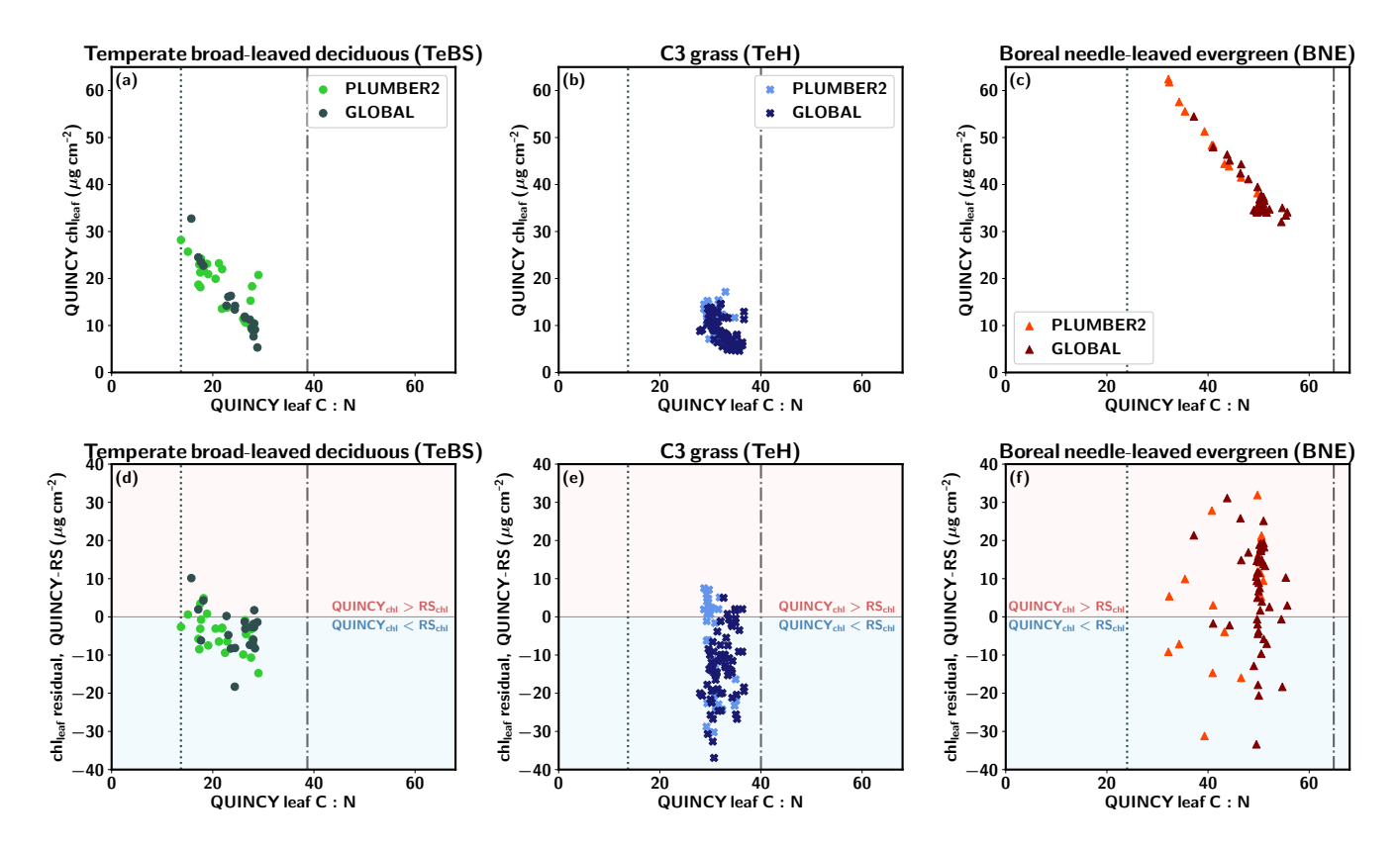


**Figure 4.** QUINCY leaf C:N and chl<sub>leaf</sub> and the corresponding residual for (**a,d**) temperate broad-leaved deciduous (TeBS), (**b,e**) C3 grass-land (**Teh**TeH) and (**c,f**) boreal needle-leaved sites (BNE). The vertical lines show the OUINCY leaf C:N minimum and maximum limits.

# 3.2 Nitrogen limitations in QUINCY

640

Figures 54a-c show the QUINCY leaf C:N ratios and the corresponding QUINCY chl<sub>leaf</sub> values for three PFTs. The TeBS sites show an almost linear relationship between chl<sub>leaf</sub> and leaf C:N with a correlation of r = -0.87 (p < 1 × 10<sup>-13</sup>). Higher leaf C:N values indicate lower leaf N levels relative to leaf C. This leads to lower chl<sub>leaf</sub> since chl<sub>leaf</sub> is a function of leaf N. The same nearly linear relationship between QUINCY leaf C:N and decreasing chl<sub>leaf</sub> is seen for the BNE sites (Fig. 54c) with a correlation of r = -0.96 (p < 1 × 10<sup>-40</sup> < 1 × 10<sup>-40</sup>). The TeH sites represent a more scattered pattern and the correlation is only r = -0.58 (p < 1 × 10<sup>-9</sup>), indicating that chl<sub>leaf</sub> is more influenced by other factorsthan leaf, such as water availability, temperature and precipitation than leaf C:N levels, compared to BNE and TeBS. However, for the TeH sites, both the QUINCY chl<sub>leaf</sub> and leaf C:N values are in a narrower range compared to the other two PFTs, which partly affects the comparison.

For the TeBS sitesites, the chl<sub>leaf</sub> residual is moderately connected to QUINCY leaf C:N values (Fig. 54d), but the same is not true for the BNE and TeH sites. Especially for the PLUMBER2 TeBS sites, the chl<sub>leaf</sub> residual is more negative for the sites with higher leaf C:N values. The TeH sites do not show much variation in the leaf C:N values, and the chl<sub>leaf</sub> residual does not appear to be connected to the magnitude of leaf C:N. The 90th percentile of TeH leaf C:N is 35.0, which is 88 % of the

QUINCY maximum leaf C:N. The BNE 90th percentile leaf C:N is 51.1 (78 % of the maximum) and the TeBS 90th percentile leaf C:N is 28.1 (73 % of the maximum value).

The majority of the GLOBAL BNE sites are clustered in a region with mean QUINCY chl<sub>leaf</sub> around 35–40  $\mu g$  cm<sup>-2</sup> and leaf C:N ratio around 50. The GLOBAL set contains more BNE sites at higher latitudes than the PLUMBER2 set (see Fig. S1). In addition, most (over 83 %) of the PLUMBER2 and GLOBAL sites with leaf C:N  $\sim$  50 are in a region with a mean annual temperature below 5 °C. The median chl<sub>leaf</sub> residual for the GLOBAL and PLUMBER2 sites is 9.9  $\mu g$  cm<sup>-2</sup> and 7.4  $\mu g$  cm<sup>-2</sup>, respectively.

We analyzed whether the chl<sub>leaf</sub> residual is connected to the GPP residual, i.e. the difference between QUINCY annual GPP and observed annual GPP (not shown). For the PLUMBER2 TeBS sites, the largest negative GPP residual, i.e. the model underestimated GPP, was for those sites that are more N-limited in QUINCY and have a negative chl<sub>leaf</sub> residual. For the PLUMBER2 TeH sites, the GPP residual was weakly negatively correlated with the chl<sub>leaf</sub> residual: the largest positive GPP residual is observed for the sites that have strong negative chl<sub>leaf</sub> residual. Similarly, the GPP residual for the PLUMBER2 BNE sites was not strongly connected with the chl<sub>leaf</sub> residual.

We also compared the QUINCY leaf C:N ratios with *in-situ* measured values for two sites (FI-Hyy and US-MMS) obtained from the TRY database. This was done to assess whether the QUINCY leaf C:N values are at a realistic level for individual sites. US-MMS is classified as a TeBS site and FI-Hyy is classified as a BNE site. For the US-MMS site, the QUINCY average leaf C:N was 17.3, and the TRY database average was 21.3. The US-MMS QUINCY leaf C:N is close to the lower leaf C:N threshold, and the QUINCY chl<sub>leaf</sub> is underestimated by 27 % compared to RS chl<sub>leaf</sub>. For the FI-Hyy site, the values were 46.5 and 38.8, respectively. The QUINCY chl<sub>leaf</sub> was underestimated by 28 %, which indicates that for FI-Hyy, there is a slightly too strong N-deficit modelled.

In order to study the effects of N limitation, we briefly analyzed the QUINCY  $C_{\rm only}$  simulation results for the PLUMBER2 BNE sites (not shown). The results revealed that at low  $chl_{\rm leaf}$  values, the difference between GPP from QUINCY default, i.e. CN, and  $C_{\rm only}$  simulations was greater than at higher  $chl_{\rm leaf}$  levels for the BNE. In addition, for the sites where the N deposition was low, the  $chl_{\rm leaf}$  values were also small.

#### 3.3 Alternative leaf Leaf N allocation schemeschemes

645

655

660

665

675

Figure 65 shows that the alternative, more realistic N allocation scheme leads, on average, to greater chl<sub>leaf</sub> and GPP underestimation for the TeBS sites compared to the QUINCY default. Furthermore, the alternative N allocation scheme produces lower leaf chl<sub>leaf</sub> (14.9 $\pm$ 4.4 µg cm<sup>-2</sup>) than the QUINCY default (17.9 $\pm$ 5.6 µg cm<sup>-2</sup>) for the PLUMBER2 TeBS sites (Fig. \$8\$10 and Table \$7\$11). The corresponding RS chl<sub>leaf</sub> mean is 22.1 $\pm$ 6.1 µg cm<sup>-2</sup>. Similarly, the TeBS mean GPP is lower for the alternative N fraction scheme, 1044 $\pm$ 311 gC m<sup>-2</sup> yr<sup>-1</sup>, while the QUINCY default mean GPP is 1231 $\pm$ 366 gC m<sup>-2</sup> yr<sup>-1</sup>. For the observations, the mean GPP is  $\pm$ 4891539 $\pm$ 375-377 gC m<sup>-2</sup> yr<sup>-1</sup>. The LAI 90th percentile values are in a similar range ( $\sim$ 4 $\pm$ 1 m<sup>2</sup> m<sup>-2</sup>) between the QUINCY default simulation and QUINCY alternative N allocation. The underestimation of GPP and chl<sub>leaf</sub> is most likely due to lower f<sub>N,rub</sub>. While the summer (JJA) f<sub>N,rub</sub> for the QUINCY default is on average 0.20 for the PLUMBER2 TeBS sites, the corresponding average for the alternative N allocation scheme is 0.09(not shown).

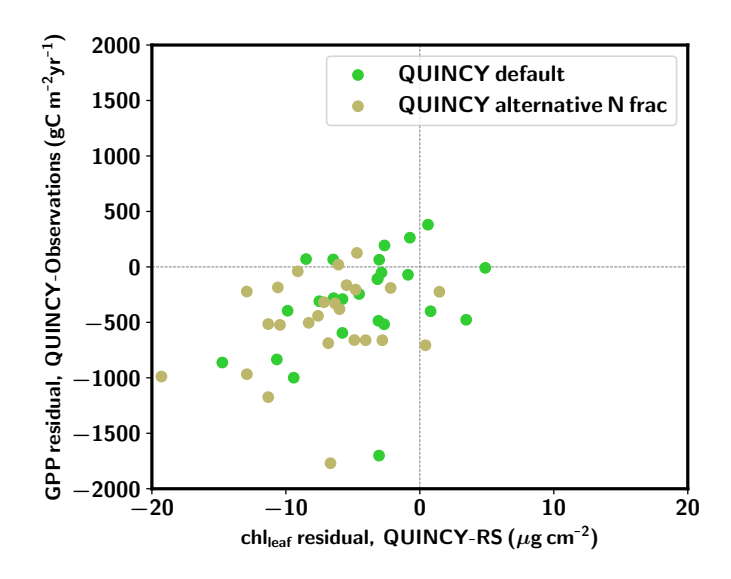


**Figure 5.** GPP residual (QUINCY - observations) versus chl<sub>leaf</sub> residual (QUINCY - observations) for the PLUMBER2 TeBS sites. The QUINCY default scheme results are marked with green circles, and QUINCY alternative N fraction results are marked with beige circles.

The results for the other PFTS PFTs were similar to those for TeBS: the  $chl_{leaf}$  and GPP magnitudes were lower with the alternative N allocation scheme (Table \$7511). An exception is the TrH sites, where the annual GPP was higher with the alternative N allocation than with the default QUINCY scheme. This was due to increased proportions of leaf N in Rubisco and electron transport, while  $f_{N,chl}$  was decreased and the  $f_{N,struct}$  slightly increased. The PFT mean values for  $f_{N,struct}$  and other fractions were calculated over sites globally, i.e. including the Southern Hemisphere sites. This affects the comparison slightly, as the seasonal cycles differ between the northern and southern hemispheres.

680

685

690

Increasing chl<sub>leaf</sub> affects more the QUINCY default chl<sub>leaf</sub> levels than QUINCY alternative N fraction output, but the difference is not large (Table \$8812). When  $f_{N,chl}$  is increased in QUINCY default, the mean chl<sub>leaf</sub> increases by 37.4 %, while the mean LAI 90th percentile decreases by 2.4 % and the mean annual GPP decreases by 6.3 %. This is due to the fact that in the QUINCY default, increasing  $f_{N,chl}$  decreases leaf N allocated in electron transport and Rubisco, since their fractions of leaf N are calculated after  $f_{N,chl}$  (see Section 2.1.12.4.1). For the alternative N fraction simulations, increasing  $f_{N,rub}$  which leads to increase in  $f_{N,chl}$  results in different dynamics compared to the QUINCY default scheme. In the alternative N allocation scheme, increasing  $f_{N,rub}$  resulted in an almost linear response in the chl<sub>leaf</sub> magnitude, with an 24.2 % increase. The increases in LAI and GPP were more moderate: 5.3 % and 12.1 %, respectively. In the QUINCY default simulation, increasing  $f_{N,chl}$  resulted in decreased GPP, while in the alternative N allocation scheme, GPP increased, Furthermore, the fraction in the structural part  $f_{N,struct}$  decreases in the alternative N allocation scheme when the  $f_{N,struct}$  but rather indirectly through its influence on leaf N, resulting in only a minor decrease of  $f_{N,struct}$ .

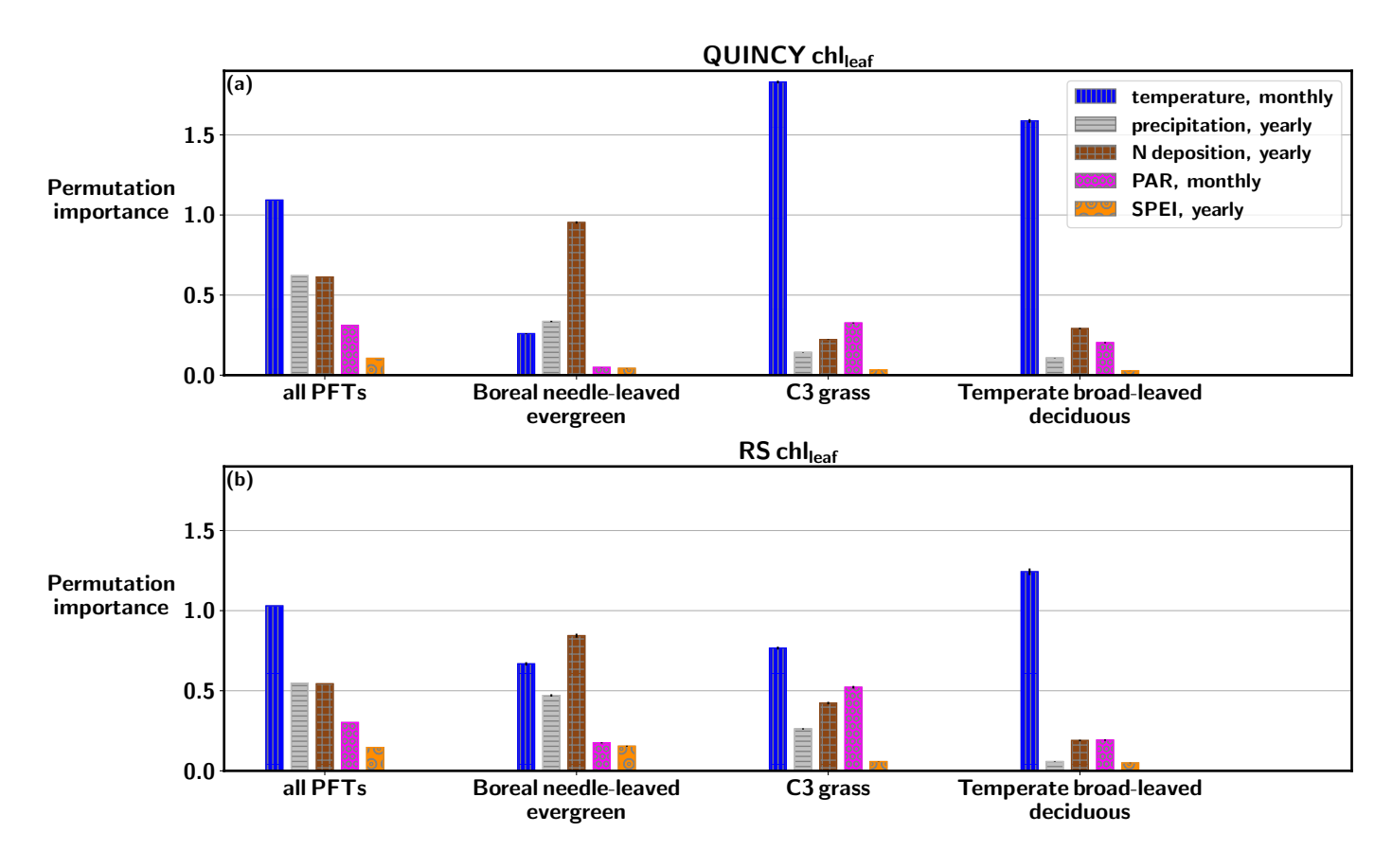


**Figure 6.** Permutation importance values based on random forest regression fitting for (a) QUINCY chl<sub>leaf</sub> and (b) RS chl<sub>leaf</sub>, based on data from all sites, and separately for BNE, TeH, and TeBS sites.

# 3.4 The environmental drivers of chl<sub>leaf</sub>

Figures 76 and \$9\$11 show that when the RF fitting is done over all PFTs, the feature importances are very similar between QUINCY and RS. Air temperature has the largest impact on the random forest fitting of both QUINCY chl<sub>leaf</sub> and RS chl<sub>leaf</sub>, when the fitting is done using data from all PFTs. The effect of air temperature is even larger for the TeH and TeBS sites compared to the importance calculated over all PFTs. This result is logical, since chl<sub>leaf</sub> is formed from leaf N, which is partly dependent on temperature via soil N mineralisation and BNFbiological nitrogen fixation (BNF). The QUINCY BNE sites do not show such a strong dependence on air temperature because the evergreen needle chl<sub>leaf</sub> does not vary as much throughout the year as deciduous chl<sub>leaf</sub>. However, temperature shows a permutation importance of 0.26±0.003 for QUINCY BNE, which is most likely a result of different sites being in different temperature regimes.

Figure \$9\$11 shows that nitrogen deposition is the most dominant driver for evergreen ecosystems for QUINCY chl<sub>leaf</sub>. For the BNE and TeNE sites, the permutation importance values are  $0.95\pm0.007$  and  $1.78\pm0.054$ , respectively, and the contribution of other environmental drivers is smaller. For the RS chl<sub>leaf</sub> of BNE sites, N deposition has the highest permutation importance

value (0.84 $\pm$ 0.012), but the role of N deposition in the RS observations is not as pronounced compared to other variables as in QUINCY. The RS chl<sub>leaf</sub> for the TeNE sites is largely driven by temperature (permutation importance = 0.63 $\pm$ 0.043). The grasslands (TeH and TrH) show similar contributions from different variables for QUINCY and RS, although RS chl<sub>leaf</sub> is less affected by temperature than QUINCY. There is a difference in the permutation importances for the TeC sites between QUINCY and RS, as QUINCY chl<sub>leaf</sub> is more influenced by temperature and RS chl<sub>leaf</sub> indicates a slightly mixed effect of different environmental drivers.

The results of the SHAP analysis (Fig. \$10\$12 and \$11\$313) are similar to the permutation importance calculations: air temperature is a dominant driver for both QUINCY and RS. In addition, the SHAP values indicate that warmer temperatures lead to higher than average chl<sub>leaf</sub> values, and colder temperatures lead to lower than average chl<sub>leaf</sub> values. The SHAP analysis for QUINCY chl<sub>leaf</sub> suggests that the higher PAR values lead to lower chl<sub>leaf</sub> values, although the majority of the data points are close to SHAP values of zero, i.e. PAR is not a strong driver of chl<sub>leaf</sub> compared to, for example, temperature. For the RS chl<sub>leaf</sub>, a similar pattern is not found, but the higher PAR would have an increasing effect on chl<sub>leaf</sub>.

# 4 Discussion

720

730

735

# 4.1 QUINCY's ability to reproduce chlleaf magnitude, LAI and GPP magnitudes

# 4.1.1 Magnitude of chlleaf

When analyzed across all sites, QUINCY chl<sub>leaf</sub> correlated well with RS observations and the PFT specific values were generally in line with the observations, and the simulated PFT-mean values were similar to RS chl<sub>leaf</sub>. In particular, the PFT mean chl<sub>leaf</sub> of the BNE and TeBS sites was close to the mean RS observations of these PFTs. However, QUINCY generally produced lower variability in chl<sub>leaf</sub> between sites compared to RS values. Particularly for C3 grasslands and crops, the QUINCY chl<sub>leaf</sub> was restricted to too narrow a range compared to RS observations. This suggests that QUINCY lacks some processes that cause variation in RS chl<sub>leaf</sub> values, and that the QUINCY dynamics for C3 grasses and crops require further in-depth analysis to explain the missing variation. In addition, the chl<sub>leaf</sub> QUINCY parameterization for C3 grasslands is the same as for trees, which could affect chl<sub>leaf</sub> dynamics. Fertilization and other management practices are not included in the version of QUINCY used in this study, which could explain the difference in the chl<sub>leaf</sub> numerical ranges between QUINCY and RS. This may affect the comparison of magnitude and seasonality for C3 cropland sites. Lu et al. (2020) gathered a collection of different chl<sub>leaf</sub> *in-situ* observations distributed globally. When comparing the QUINCY chl<sub>leaf</sub> values with those reported by Lu et al. (2020), it was observed that C3 crops and C3 grasslands are most likely underestimated, similarly when compared to the RS chl<sub>leaf</sub> values. The correlation between QUINCY chl<sub>leaf</sub> and RS chl<sub>leaf</sub> was poor for C3 grasslands and C3 crops. This also highlights the need for tuning the QUINCY parameterization for grasslands, and possibly other changes to the model structure to capture the grassland chl<sub>leaf</sub> dynamics.

Some of the PLUMBER2 sites are located in fens and wetlands, and these are classified as C3 grasslands in QUINCY. The model version of QUINCY used in this study does not include wetlands or fens, and therefore for some of the sites (e.g. FI-Lom

in high latitude region) QUINCY does not model the relevant water table depth dynamics, which may influence the carbon and water dynamics at the sites.

For C4 plants, the range for QUINCY values was similar to RS chl<sub>leaf</sub> for higher values, but lower chl<sub>leaf</sub> concentrations were missing in QUINCY. Lu et al. (2020) reported 15–60 µg cm<sup>-2</sup>, while the QUINCY chl<sub>leaf</sub> range for C4 grasslands was 31–72 µg cm<sup>-2</sup>. The RS chl<sub>leaf</sub> range for C4 grasslands was 12–63 µg cm<sup>-2</sup>. However, it should be noted that QUINCY chl<sub>leaf</sub> values only represent the top of the canopy, while *in-situ* observations may have mixed results from different canopy heights, which may affect the comparison.

For the BNE sites, the QUINCY chl<sub>leaf</sub> overestimation was higher for GLOBAL than PLUMBER sites, and relatively higher portion of GLOBAL BNE sites were located in high latitudes. This suggests that the QUINCY chl<sub>leaf</sub> overestimation or RS chl<sub>leaf</sub> underestimation, is more pronounced for the needle-leaved sites in cold regions, which could partly reflect the challenges of optical remote sensing in high latitudes.

Our machine learning-based analysis indicated that QUINCY is able to capture the influence of environmental drivers of the chl<sub>leaf</sub> in a big picture. QUINCY chl<sub>leaf</sub> for evergreen sites was driven by N deposition, with other environmental variables contributing less. The same was true for the RS chl<sub>leaf</sub> for BNE and TrBE but not for TeNE. Additional comparison of QUINCY simulations with active C and N cycles with a C<sub>oulx</sub> simulation also demonstrated a similar conclusion. Though, the RS chl<sub>leaf</sub> for BNE sites seemed to be more temperature-driven than for QUINCY. This could be explained by differences in the seasonal cycle, as RS chl<sub>leaf</sub> shows a seasonal pattern for BNE sites, while QUINCY does not. In addition, it was observed that QUINCY chl<sub>leaf</sub> for the TeC sites was mainly driven by temperature, while RS chl<sub>leaf</sub> had more equal contributions from different variables. In addition, the footprint size of RS chl<sub>leaf</sub> may affect the comparison, as crops are typically located in a heterogeneous landscape. The analysis with the SHAP values revealed that higher PAR values could produce lower chl<sub>leaf</sub> in QUINCY simulations. The decreasing effect of higher PAR values on QUINCY chl<sub>leaf</sub> could be partly due to the tropical regions, where the PAR radiation does not vary as much throughout the year. The decreasing effect could be also attributed to differences between different sites.

## 4.1.2 Magnitudes of LAI and GPP

750

755

760

765

770

The QUINCY annual GPP showed a good correlation with ground station observations, but the QUINCY underestimated the annual GPP for PLUMBER2 observations, however, the values were underestimated at most of the PLUMBER2 sites. This could be partly due to a slightly delayed growing season for the deciduous forests (Fig. S6S8), which hinders the early spring carbon sequestration. The delayed seasonal development calls for tuning the QUINCY phenology parameters, which could benefit the simulations with a reasonable amount of work. However, for some of the PFTs (TeC, TrBR, TeBE), QUINCY overestimated GPP.

The simulated LAI over all PFTs was generally in an agreement with RS LAI (Fig. S3d and Table S8). However, a clear future development point for QUINCY is the overestimation of LAI values, which was the case for most of the PFTs. The overestimation of LAI in QUINCY could be due to, for instance, missing herbivores and management. These effects are currently under development in QUINCY. The overestimation of LAI is pronounced for the C4 grasslands, for which the

LAI values in QUINCY were unrealistically high. The very high LAI values were observed for the GLOBAL sites located on the African and South American continents, for which we did not have GPP ground station data. However, the QUINCY GPP for the PLUMBER2 C4 grassland sites was within a reasonable range, and the QUINCY PFT mean GPP was close to the observed PFT mean GPP. This suggests that despite high LAI, QUINCY is able to account for environmental conditions affecting GPP and maintain realistic GPP levels. However, for the GLOBAL TrH C4 grassland (TrH) sites, it was observed that if the simulated extremely high LAI values were coupled with high chl<sub>leaf</sub>, this resulted in high simulated GPP in the modelyalues. The RS observations could potentially be used in model tuning to balance the overestimation of both LAI and chl<sub>leaf</sub>.

The underestimation of GPP in the Hainich forest (Section 3.1.1) was most likely due to a too low LAI, as the QUINCY

V<sub>c(max)</sub> seemed to be in a reasonable range compared to observations at the site (Legner, 2012; Knohl and Baldocchi, 2008).

The QUINCY JJA LAI value was underestimated compared to RS JJA LAI and also to the values presented by Knohl and Baldocchi (2008) and Forrester et al. (2016). The delayed seasonal cycle of GPP partly explains the underestimation of the annual QUINCY

GPP at the Hainich site. However, although the simulated LAI showed delayed decline in autumn, the GPP decreased due to

environmental drivers. This indicates that QUINCY is able to maintain reasonable GPP levels in autumn even when LAI is overestimated.

Although QUINCY tended to overestimate LAI in general, it tended to underestimate LAI for TeBS ecosystems (Fig. S3d and Table S5) for TeBS it was mostly underestimated. Similarly, the QUINCY mean chl<sub>leaf</sub> is underestimated at the majority of the the TeBS sites. However, when analyzing the residuals for individual sites, the GPP under- or overestimation was not always related to the chl<sub>leaf</sub> or LAI residual. Less than half of the 25 PLUMBER2 TeBS sites showed an underestimation for all chl<sub>leaf</sub>, LAI, and GPP. Overestimation of LAI can potentially lead to too strong shading, which can result in too small could result in reduced GPP in lower canopy layers. In addition, the The radiative transfer model might therefore play a role in the underestimated GPP.

790

800

805

Furthermore, it was observed that the QUINCY chl<sub>leaf</sub> overestimation was higher for GLOBAL BNE sites than PLUMBER2 BNE sites, and relatively higher portion of GLOBAL BNE sites were located in high latitudes. This suggests that the QUINCY chl<sub>leaf</sub> overestimation or RS chl<sub>leaf</sub> underestimation, is pronounced for the needle-leaved sites in cold regions, which could partly reflect the challenges of optical remote sensing in high latitudes.

Some of the PLUMBER2 sites are located in croplands, fens and wetlands, and these are classified as C3 grasslands in QUINCY. The model version of QUINCY used in this study does not include wetlands or fens, and therefore for some of the sites (e.g. FI-Lom in high latitude region) QUINCY does not model the relevant water table depth dynamics, which may influence the carbon and water dynamics at the sites. Another missing processes in are fertilization and management of croplands. Fertilization and other management practices are not included in the version of QUINCY used in this study, which could explain the difference in the chl<sub>leaf</sub> numerical ranges between QUINCY and RS. This may affect the comparison of magnitude and seasonality for C3 cropland sites. Lu et al. (2020) gathered a collection of different chl<sub>leaf</sub> *in-situ* observations distributed globally. When comparing the QUINCY chl<sub>leaf</sub> values with those reported by Lu et al. (2020), it was observed that C3 crops and C3 grasslands are most likely underestimated, similarly when compared to the RS chl<sub>leaf</sub> values. The correlation

between QUINCY chl<sub>leaf</sub> and RS chl<sub>leaf</sub> was poor for C3 grasslands and C3 crops. This also highlights the need for tuning the QUINCY parameterization for grasslands, and possibly other changes to the model structure to capture the grassland chl<sub>leaf</sub> dynamics.

For C4 plants, QUINCY values were in a similar range at the higher values, but lower chl<sub>leaf</sub> concentrations were missing.

Lu et al. (2020) reported 15–60, while the QUINCY chl<sub>leaf</sub> range for C4 grasslands was 31–72However, it should be noted that QUINCY chl<sub>leaf</sub> values only represent the top of the canopy, while *in-situ* observations may have mixed results from different canopy heights, which may affect the comparison.

Our analysis using the more advanced N allocation routine shows that the chl<sub>leaf</sub> and GPP magnitude for the TeBS sites were not improved compared to the observation data. This was partly due to lower f<sub>N,rub</sub>. In the alternative N scheme, f<sub>N,chl</sub> is a function of f<sub>N,et</sub> and therefore a function of f<sub>N,rub</sub>, and therefore the lower f<sub>N,rub</sub> affects both GPP and chl<sub>leaf</sub>. The underestimation of f<sub>N,rub</sub> could be partly due to the LMA representation in QUINCY. LMA is the inverse of SLA, and thus it is the same fixed value for all PFTs, which may be too general a representation with respect to the N allocation scheme. On the other hand, the advanced N allocation scheme provided a more realistic mechanism when f<sub>N,chl</sub> was increased. This indicates that the alternative N allocation scheme produces more in line with our current ecophysiological understanding of plant dynamics: increasing leaf N in chl<sub>leaf</sub> does not decrease other photosynthetic fractions, but more structural part (f<sub>N,struct</sub>).

Our machine learning based analysis indicated that QUINCY is able to capture the influence of environmental drivers of the ehl<sub>leaf</sub> in a big picture. QUINCY chl<sub>leaf</sub> for evergreen sites was driven by N deposition, with other environmental variables contributing less. The same was true for the RS chl<sub>leaf</sub> for BNE and TrBR, but not for TeNE. Additional comparison of QUINCY simulations with active C and N eyeles with a C<sub>only</sub> simulation also demonstrated a similar conclusion. Though, the RS chl<sub>leaf</sub> for BNE sites seemed to be more temperature-driven than for QUINCY. This could be explained by differences in the seasonal cycle, as RS chl<sub>leaf</sub> shows a seasonal pattern for BNE sites, while QUINCY does not. In addition, it was observed that QUINCY chl<sub>leaf</sub> for the TeC sites was mainly driven by temperature, while RS chl<sub>leaf</sub> had more equal contributions from different variables. In addition, the footprint size of RS chl<sub>leaf</sub> may affect the comparison, as crops are typically located in a heterogeneous landscape. The analysis with the SHAP values revealed that higher PAR values could produce lower chl<sub>leaf</sub> in QUINCY simulations. The decreasing effect of higher PAR values on QUINCY chl<sub>leaf</sub> could be partly due to the tropical regions, where the PAR radiation does not vary as much throughout the year. The decreasing effect could be also attributed to differences between different sites.

## 4.2 QUINCY's ability to reproduce the **chlical** observed seasonal cycle

825

830

840

The seasonality of GPP for QUINCY was consistent with the observations for many of the PFTs. However, the seasonality for chl<sub>leaf</sub> and LAI in QUINCY was found to have differences compared to RS values for some of the PFTs.

The annual cycle of QUINCY chl<sub>leaf</sub> for deciduous forest sites was similar when QUINCY and RS chl<sub>leaf</sub> were compared. However, the increase in spring chl<sub>leaf</sub> in QUINCY chl<sub>leaf</sub> occurred late compared to RS chl<sub>leaf</sub>, as well as decrease in autumn chl<sub>leaf</sub>. The QUINCY LAI estimations showed similar biases when compared against RS results. this was not reflected as prominently in the seasonality of GPP compared to the delay in LAI, most likely due to environmental drivers. This indicates

that QUINCY is able to maintain reasonable GPP levels in autumn even when LAI is overestimated. For the NH PLUMBER2 TeBS sites, the PFT-averaged seasonal cycle showed that the QUINCY underestimation of annual GPP is not too strongly affected by the delay in start of the growing season. The GPP sum for the spring (MAM) was underestimated by QUINCY by  $\sim 93 \text{ gC m}^{-2}$ , while the overestimation in the autumn (SON) was  $95 \text{ gC m}^{-2}$ , i.e. they compensate each other.

The QUINCY chl<sub>leaf</sub> and LAI seasonality differed from RS observations for the boreal and temperate evergreen sites. 845 QUINCY chl<sub>leaf</sub> and LAI do not change as much from season to season at these evergreen sites, whereas RS chl<sub>leaf</sub> and LAI show more variation during the year. The RS chlleaf for BNE forests implied a stronger seasonal cycle than what was seen from *in-situ* observations at two BNE sites, which was most likely driven by too strong LAI seasonality of the RS product. Demmig-Adams et al. (2014) reported that for Korean fir trees, spring chl<sub>leaf</sub> was higher than winter, and summer chl<sub>leaf</sub> was 850 slightly higher than winter values. In addition, the RS observations for the Sodankylä site indicated that there would be a small (FI-Sod) and Niwot Ridge (US-NR1) sites indicated a slight decrease in spring chl<sub>leaf</sub>, which and this was seen also for other BNE sites. The decrease in RS chl<sub>leaf</sub> in spring could be driven by resorption of N to form new needles, or by understory impact the impact of the understory during the snow-melt season. A study by Zhang et al. (2019), conducted in a laboratory environment, demonstrated a similar decrease for a boreal evergreen forest. The RS chl<sub>leaf</sub> retrieval algorithm does 855 not consider variations in understory, and therefore the understory vegetation can cause artifacts to the retrieved needle-leaf reflectance signal. Similar effect was observed for the RS chl<sub>leaf</sub> for For US-NR1, the mountainous landscape might affect the retrieval. In addition, the mountainous landscape surrounding US-NR1 might affect RS retrieval, which also can create artifacts to the mean RS chl<sub>leaf</sub> after DOY 200. A study by Zhang et al. (2019), conducted in a laboratory environment, demonstrated a similar decrease for a boreal evergreen forest. The Sentinel-3 chl<sub>leaf</sub> shows the strongest seasonal cycle at the US-NR1 site compared to other products used in this study, which could be partly due to assumptions made in the retrieval processing. For 860 instance, the assumptions made for the LAI seasonality and the effect of snow cover can affect the RS chleaf retrieval. For temperate broad-leaved evergreen sites, QUINCY did not simulate seasonal variation in chleaf, while RS chleaf showed a clear increase in spring and decrease in fall. Site-level studies have indicated contradicting results for chl<sub>leaf</sub> seasonal cycle for temperate evergreen forests (Joshi et al., 2024; Yasumura and Ishida, 2011), therefore it is not straightforward judge whether 865 the model behavior is erroneous.

The *in-situ* observations in the boreal Sodankylä forest (Fig. 43a) for the year 2015 showed that the chl<sub>leaf</sub> concentrations increased throughout the growing season in needle-leaved forests. Similar behavior at other evergreen needle-leaved forests was reported by Laitinen et al. (2000) and Katahata et al. (2007). The increase in chl<sub>leaf</sub> could indicate that the Sodankylä forest may be N-limited, and requires strong N uptake throughout the summer. However, the The observations from the Niwot Ridge forest did not show such a strong pattern (Fig. \$7\$9), as also shown by Bowling et al. (2018) , potentially reflecting a different N status of the ecosystem. The Sentinel-3 chl<sub>leaf</sub> shows the strongest seasonal cycle for the US-NR1 compared to other products used in this study, which could be partly due to assumptions made in the retrieval processing. For temperate broad-leaved evergreen sites , QUINCY did not simulate seasonal variation in chl<sub>leaf</sub>, while RS chl<sub>leaf</sub> showed a clear increase in spring and decrease in fall. A study by Yasumura and Ishida (2011) found no seasonal pattern observed for a broad-leaved

870

evergreen site while a study by Joshi et al. (2024) concluded that there is a clear seasonal change in chl<sub>leaf</sub> for temperate evergreen trees

For TeC and TeH sites, the seasonal cycle of QUINCY chl<sub>leaf</sub> was delayed compared to RS, but the bias was not large. The lower QUINCY spring chl<sub>leaf</sub> for NH TrH sites suggests that the phenological cycle for these sites needs further tuning in QUINCY, and is most likely linked to simulated LAI biases. In QUINCY, the start of senescence is controlled by soil moisture and temperature thresholds. Given the high species diversity in herbaceous systems, both within and between sites, ecosystem-level models such as QUINCY often struggle to capture phenological variation. This is partially due to PFT-level parameters not reflecting diversity at the site level, and partially due to the difficulty of capturing an average response of diverse species.

# 4.3 Modeling the N cycle and N limitation

880

895

905

QUINCY is one of the state-of-the art TBMs that includes include an advanced representation of chl<sub>leaf</sub> in the canopy, and also the connection between chl<sub>leaf</sub> and N limitation. This allows the intercomparison to Earth observation remote sensing chl<sub>leaf</sub> products, which can be further extended to cover analysing the N limitation on photosynthesis and the implications on carbon sequestration efficiency. In addition, our analysis demonstrated how to use chl<sub>leaf</sub> as a metric to support analysing the N limitation in simulations. ThoughHowever, one needs to keep in mind that the modelled and remotely sensed chl<sub>leaf</sub> are not completely equivalent, but there are conceptual differences in spatial coverage, for instance.

The strongest QUINCY GPP underestimation for the PLUMBER2 TeBS sites was connected to stronger N-limitation and QUINCY chl<sub>leaf</sub> underestimation, suggesting to a too strong modeled N limitation for these sites. However, as Fig. 5d shows, the leaf C:N values were not close to the maximum leaf C:N values for the TeBS sites, suggesting that the QUINCY maximum threshold value of leaf C:N may be slightly too high. In addition, the results in Fig. 5d suggest that for some of the TeBS sites, the QUINCY chl<sub>leaf</sub> underestimation could be due to lower N availability or allocation to leaves (Fig. 4d). Though, we compared QUINCY leaf C:N values to the TRY database observation leaf C:N values for two sites, and the QUINCY values were in line with the observations.

Some of the QUINCY chl<sub>leaf</sub> underestimation for the TeBS sites could be due to lower N availability or allocation to leaves (Fig. 4d). Both the QUINCY underestimation of chl<sub>leaf</sub>, and also GPP couldThe QUINCY underestimation of GPP could also be partly related to modeling deficiencies in the N cycle. The QUINCY mean symbiotic BNF was ~0.3 gNm<sup>-2</sup>yr<sup>-1</sup> for the TeBS sites. Davies-Barnard and Friedlingstein (2020) report that for deciduous broad-leaved forests, including both tropical and temperate forests, the mean symbiotic BNF is approximately 0.8 gNm<sup>-2</sup>yr<sup>-1</sup>, suggesting that QUINCY symbiotic BNF is underestimated for the TeBS sites. However, as discussed in Section 3.2, at least the PLUMBER2 TeBS sites do not appear to be highly N-limited in QUINCY as the leaf C:N maximum threshold is not reached. Though, the negative residual of chl<sub>leaf</sub> between model and observations was higher with the higher leaf C:N values, indicating that QUINCY's modeled N deficit for the TeBS sites is too strong. The analysis shows that for the TeBS forests, the chl<sub>leaf</sub> residual between simulated and RS chl<sub>leaf</sub> brings additional information in pinpointing that the N-deficit influence is overestimated at the certain sites and contributing to too low GPP.

For the BNE sites, QUINCY overestimated chl<sub>leaf</sub> compared to RS chl<sub>leaf</sub>, and the BNE chl<sub>leaf</sub> and GPP residuals were not correlating, which may be partly be due to RS chl<sub>leaf</sub> magnitude issues as presented in Section 3.1.23.1.3. The observed GPP increased as a function of observed chl<sub>leaf</sub> (not shown), and this was also evident in the simulations. A comparison of QUINCY CN- and C-only simulations for the BNE sites indicated that QUINCY simulates an N deficit at low chl<sub>leaf</sub> values. The observed GPP increased as a function of observed chl<sub>leaf</sub>, and this was also evident in the simulations, as GPP was lower with the CN-simulation. Including the N cycle in the simulations improved the model behavior and led to a decrease in simulated chl<sub>leaf</sub> values at the lower end of the observations and improved model behavior in terms of chl<sub>leaf</sub> and GPP. This shows a realistic behavior of the QUINCY N cycle. Furthermore, the low chl<sub>leaf</sub> values coincided with the low N deposition values, indicating that N deposition plays a significant role in the N deficit of these ecosystems, as also shown in the feature importance analysis results.

In addition, the TeH leaf C:N values (Fig. 54e) were closer to the upper bound and covering only approximately half of the leaf C:N range derived from the TRY database, even if when we had sites globally distributed across different climatological regions. This suggests that many of the TeH sites are more N-limited in QUINCY compared to BNE and TeBS sites, and that QUINCY has difficulty capturing TeH sites with high leaf N values. This may be a partial cause of the too low and also too static chl<sub>leaf</sub> values for the TeH sites. For the TeH sites, QUINCY had the largest overestimation of GPP when the modeled chl<sub>leaf</sub> is the most underestimated. This indicates that the leaf N allocation in QUINCY for TeH sites requires further parameter tuning. The QUINCY dynamics related to N cycling may require further analysis , to estimate the contributions of N deposition and BNF to leaf N contentand, and to determine whether they are in the range of estimates presented in the reference literature.

Our analysis using the more advanced N allocation routine shows that the  $chl_{leaf}$  and GPP magnitudes for the TeBS sites were not improved compared to the observation data. This was partly due to lower  $f_{N,rub}$ . In the alternative N scheme,  $f_{N,chl}$  is a function of  $f_{N,chl}$  and therefore a function of  $f_{N,rub}$ , and therefore the lower  $f_{N,rub}$  affects both GPP and  $chl_{leaf}$ . The underestimation of  $f_{N,rub}$  could be partly due to the LMA representation in QUINCY. LMA is the inverse of SLA, and thus it is the same fixed value per PFT, which may be too general a representation with respect to the N allocation scheme. On the other hand, the advanced N allocation scheme provided a more realistic mechanism when  $f_{N,rub}$  was increased by resulting in simultaneous increases in  $f_{N,chl}$  and GPP. This indicates that what the alternative N allocation scheme produces is more in line with the current ecophysiological understanding from the literature (Onoda et al., 2017; Evans and Clarke, 2019) regarding the relationship between  $V_{C(max)}$  and  $chl_{leaf}$ : increasing leaf N in  $chl_{leaf}$  does not decrease other photosynthetic fractions, but rather the structural part ( $f_{N,struct}$ ).

#### 4.4 Limitations of the analysis

910

915

920

925

930

935

# 4.4.1 Limitations due to remote sensing products

Although the satellite product by Croft et al. (2020) agrees well with the *in-situ* observations (Croft et al., 2020), the satellite retrieval products contain a certain degree of uncertainty. As Boegh et al. (2013) conclude, satellite inversions are often ill-posed inversion problems, which can complicate the retrieval of chl<sub>leaf</sub> and LAI from remote sensing data. Furthermore, the

coverage of the MERIS satellite data is not optimal for certain regions such as South America, the tropics, western Australia, and parts of the boreal zone. This is partly due to gaps in the original data caused by clouds, sensor errors, or light conditions (Tum et al., 2016). The influence of gaps has been partially minimized in , though the RS chl<sub>leaf</sub> by Croft et al. (2020) by gap-filling the missing data with the year 2010 data and product by Croft et al. (2020) is gap-filled with a smoothing algorithm. In addition, in this study, the impact of gaps has been partially reduced by using the average of all years.

Our analysis relied primarily on one RS chl<sub>leaf</sub> product. For example, RS observations from the Sentinel-3 satellite could be included as it was they were tested for two sites in this study, although the time periods of the modeled values did not match these observations. The challenge with Sentinel-3 is that the *in-situ* observations are often provided years back in time, and Sentinel-3 has only been operational since 2016. A potential candidate for combination with Sentinel-based chl<sub>leaf</sub> products could be ICOS observations. The European ICOS research infrastructure provides up-to-date flux measurements that are also harmonized in terms of measurement and post-processing techniques.

The remote sensing products of LAI are known to have an overly pronounced seasonal cycle in the boreal needle-leaved forests, with LAI values being underestimated in winter, early spring and late fall (Heiskanen et al., 2012; Wang et al., 2019). This is caused by snow and cloud contamination, the understory effects, seasonal variation in needle greenness, low solar zenith angle and poor illumination (Heiskanen et al., 2012; Fang et al., 2013; Wang et al., 2019). In our study, we observed that for the Sodankylä BNE forest, RS LAI showed a clear seasonal pattern, while QUINCY LAI was almost constant throughout the season. We also compared QUINCY fAPAR with in-situ measurements, and this comparison revealed that QUINCY fAPAR followed the *in-situ* measurements outside the winter season. The *in-situ* measurements during the winter season were influenced by the low elevation angles of the sun, which limits limit the reliability of the measurements throughout the winter months and, in mid-winter, results in polar night. Additionally, in late spring, ground-level sensors may be covered by snow, compromising data quality even when light conditions would otherwise be sufficient. In addition, as Wang et al. (2024) show, RS-based data often contain inaccuracies in autumn phenology. In our analysis, we used ground-based flux tower observations, which helped to form a comprehensive view of model performance. Croft et al. (2020) report that the RS chl<sub>leaf</sub> for the needle-leaved forests could benefit from intra-PFT variability in the structural parameters (e.g. canopy height, stem density), which would improve the spatial variability in chl<sub>leaf</sub>. The contemporary RS products are advancing in this front, providing opportunities to improve other RS products. However, the Sentinel-3 product used in this study was not yet free of these problems.

#### 4.4.2 Limitations due to ground based observations

945

950

955

960

965

970 The flux tower measurements used in this study were not evenly distributed geographically, but rather concentrated in central Europe and the United States. For example, the number of sites in Central and South America was small, limiting the comprehensiveness of the analysis of the GPP magnitudes relative to ground observations. TBMs and RS products cover larger spatial areas, allowing a global assessment even in areas where the *in-situ* observations are sparse. In this study, we were able to first analyze data at sites where we had ground station measurements (PLUMBER2), and then extend to other regions without *in-situ* observations (GLOBAL).

QUINCY simulations are based on the assumption of an average individual plant or a tree, and do not consider plants of different ages. Similarly, RS inversion algorithm does not consider variations in, for instance, tree height or crown width. As previous studies have shown, chl<sub>leaf</sub> and nitrogen concentrations in leaves can vary between trees of different ages and also between individuals (Laitinen et al., 2000; Sallas et al., 2003; Warren and Adams, 2001; Thurner et al., 2025). In addition, PFT can be a very broad category and different tree species may have different characteristics, which is taken into account in our PFT-based modeling scheme and parameterization. Furthermore, the modeling framework does not account for competition among plants.

In addition, our analysis does not take into account the potential footprint mismatch between RS chl<sub>leaf</sub> and the flux towers at the ground stations. Furthermore, the flux tower footprints are not always homogeneous, but represent a mixture of e.g. shrubs and trees. Our QUINCY modeling scheme assumed only one PFT for each of the sites, which may lead to differences in the GPP if the flux tower site is located between is surrounded by heterogeneous plant cover. For some sites, we increased the footprint area of the RS chl<sub>leaf</sub> to include pixels with the same land cover classification. This increase may have resulted in greater differences in the footprint compared to the flux tower footprint. Site location, topography, and landscape heterogeneity influence the measured CO<sub>2</sub> fluxes (Giannico et al., 2018; Griebel et al., 2016).

# 4.4.3 Limitations of QUINCY and data-analysis

980

985

990

995

1000

1005

QUINCY simulations are based on the assumption of an average individual plant or a tree, and do not consider plants of different ages. Similarly, RS inversion algorithms do not consider variations in, for instance, tree height or crown width. As previous studies have shown, chl<sub>leaf</sub> and nitrogen concentrations in leaves can vary between trees of different ages and also between individuals (Laitinen et al., 2000; Sallas et al., 2003; Warren and Adams, 2001; Thurner et al., 2025). In addition, a PFT can be a very broad category and different tree species may have different characteristics, which is not taken into account in our PFT-based modeling scheme and parameterization. Furthermore, the modeling framework does not account for competition among plants.

Land cover classification can introduce an additional source of uncertainty in this study. There are two sources of uncertainty in the use of land cover maps, as they can be caused by the classification into land cover classes based on spectral reflectance or by the conversion of these land cover classes into the PFT classes that we used (Georgievski and Hagemann, 2019). We have partially accounted for this uncertainty by increasing the number of points that we used for each of the study sites.

The SHAP value analysis with RF fitting resulted in differing results between QUINCY and RS chl<sub>leaf</sub> and the impact of PAR values on chl<sub>leaf</sub>. Since the SHAP values only describe the machine learning interpretation of the variable relationships, further investigation of the effect of high PAR values on QUINCY chl<sub>leaf</sub> would require additional QUINCY simulations where the radiation input fields are increased, but keeping the rest of the input variables the same.

Our analysis could also benefit from including local measurements of *in-situ* greenness indices (Linkosalmi et al., 2016) to further validate the seasonal cycle of chl<sub>leaf</sub> for different PFTs, or up-scaled leaf trait maps (Dechant et al., 2024). For instance, the up-scaled maps could provide regional, PFT-specific SLA values that could improve the results of the alternative N allocation scheme.

#### 1010 5 Future directions

1015

1025

1030

1035

1040

#### 4.5 Future directions

One objective of this study was to estimate the gain of using RS chl<sub>leaf</sub> to improve the modeled carbon and nitrogen cycle. However, the approach in this study is based on only one TBM. Though, our analysis included a comparison of two different chl<sub>leaf</sub> formulations within a model, which has the advantage that the comparison is not masked out by differences in dynamics between the two models. As recommended by Meyerholt et al. (2020), a model ensemble would provide more robust results, as there is some uncertainty in a single process model approach. However, this would be possible only if other TBMs were to provide chl<sub>leaf</sub> as a diagnostic, which would also allow that chl<sub>leaf</sub> could potentially be incorporated into TBM benchmarking platforms, such as ILAMB (Collier et al., 2018).

Another future prospect could be to integrate QUINCY into a digital framework that integrates RS observational time series,

TBMs and a radiative transfer model. Based on a comprehensive literature review, Kooistra et al. (2024) propose that such a
digital twin combination with data assimilation could enable an almost near-time near-real-time representation of ecosystems
and help to overcome the current modeling limitations.

#### 5 Conclusions

The evaluation revealed that the magnitudes of QUINCY chl<sub>leaf</sub> correlate well with RS chl<sub>leaf</sub> when analyzed across all plant functional types. However, for some of the PFTs, the QUINCY chl<sub>leaf</sub> values showed less site-to-site variation compared to the observations. This suggests that the QUINCY parameterization requires further adjustments. RS chl<sub>leaf</sub> for needle-leaved sites was clearly lower than for QUINCY. The comparison to *in-situ* chl<sub>leaf</sub> measurements indicated that RS chl<sub>leaf</sub> is underestimated for the boreal coniferous forests, while QUINCY chl<sub>leaf</sub> was in a reasonable magnitude. The inter-comparison of QUINCY and RS chl<sub>leaf</sub> and LAI seasonal cycles showed that QUINCY produced delayed seasonal pattern for deciduous tress. This suggests that the phenological parameters of QUINCY need further adjustment. In addition, for evergreen needle-leaved forests, there was a clear seasonal pattern in RS chl<sub>leaf</sub> and LAI, while QUINCY LAI and chl<sub>leaf</sub> did not vary much throughout the annual cycle. However, the comparison to *in-situ* chl<sub>leaf</sub> demonstrated that the RS chl<sub>leaf</sub> overestimates seasonality of chl<sub>leaf</sub> for needle-leaved evergreen forests in cold environments, which is likely caused by the RS LAI biases (Heiskanen et al., 2012; Wang et al., 2019) known to happen in these regions. Our analysis highlighted that while QUINCY was able to produce chl<sub>leaf</sub> magnitudes in the big picture, the representation of chl<sub>leaf</sub> in QUINCY calls for further improvement. In addition, the results from machine learning-based regression indicated that QUINCY and RS chl<sub>leaf</sub> have similar contributions from different environmental drivers when the analysis was performed over all sites and PFTs.

We also tested an alternative leaf N allocation scheme, which resulted in more realistic ecophysiological behaviour. A follow-up study with adjusting the parameterization to have a better match with observations, and a larger sample of sites would provide valuable insights into the benefits of using the alternative N allocation scheme.

Our results reveal that adding chl<sub>leaf</sub> to the model evaluation provides additional information on photosynthetic processes and leaf N distribution compared to using LAI alone. While LAI provides information about seasonality, information based on chl<sub>leaf</sub> complements this by enabling us to address the N status of the leaves and identify the main drivers of the chl<sub>leaf</sub> content. In this paper, we have demonstrated the applicability of using remotely sensed chl<sub>leaf</sub> as an evaluation point for TBMs. Our study highlights the potential of the use of RS chl<sub>leaf</sub> as a model evaluation tool for analysing the C and N cycles.

Code and data availability. The QUINCY model codes are available under a GPL v3 license. The scientific code of QUINCY relies on software infrastructure from the MPI-ESM environment, which is subject to the MPI-M License Agreement in its most recent form (https://www.bgc-jena.mpg.de/en/bsi/projects/quincy/software), last access: 3 June, 2025). The source code is available online https://doi.org/10.17871/quincy-model-2019, release 76b2549 (last access: 3 June, 2025), but access is limited to registered users. Readers interested in running the model should request a username and password via the Git repository. Model users are strongly encouraged to follow the fair-use policy (https://www.bgc-jena.mpg.de/en/bsi/projects/quincy/software, las access: 3 June, 2025last access: 3 June, 2025). The QUINCY simulated data used in this study are available at https://doi.org/10.57707/fmi-b2share.6a3849a7694b4f4a9efba39abde734af (Miinalainen and Thum, 2025) (Last access: 11 June, 2025).https://doi.org/10.57707/fmi-b2share.f8ab5f4ed6534b1597a2db73cc5175ff (Miinalainen et al., 2025) (Last access: 6 October, 2025). The forcing data to run the QUINCY model are stored in the model repository.

The global drought monitoring SPEI data is available in https://global-drought-crops.csic.es/#map\_name=all\_spei\_0.5#map\_position= 2211 (Last access 3 June, 2025).

RS chl<sub>leaf</sub> by Croft et al. (2020) will be available by request from the authors. The post-processed RS chl<sub>leaf</sub> (Croft et al., 2020) for the PLUMBER2 and GLOBAL sites is available at https://doi.org/10.57707/fmi-b2share.f8ab5f4ed6534b1597a2db73cc5175ff (Miinalainen et al., 2025) (Last access: 6 October, 2025).

The Sodankylä chl<sub>leaf</sub> *in-situ* measurement data is available by request from the authors and will be published in an open data repository in https://zenodo.org/records/17192030 (Peltoniemi et al., 2025) (Last access: 24 September, 2025).

The Sodankylä fAPAR measurement data is available by request from the authors, and will be published in an open data repository at https://doi.org/10.57707/fmi-b2share.f8ab5f4ed6534b1597a2db73cc5175ff (Miinalainen et al., 2025) (Last access: 6 October, 2025)...

The Sentinel3 RS chl<sub>leaf</sub> can be retrieved using the scripts available from here: https://github.com/psreyes/S3\_TOA\_GPR\_1.git (Last access: 3 June, 2025)

Author contributions. TT, TM and SZ designed the study. AO and TM wrote scripts for the data analysis. MA collected the Sodankylä fAPAR data. MP provided the Sodankylä leaf chl<sub>leaf</sub> data. HC provided the remote sensing chl<sub>leaf</sub> data. TM drafted the manuscript stem. All authors participated in the interpretation of the results and manuscript writing.

1070 Competing interests. The authors declare no competing interests.

1045

1050

Acknowledgements. TM and TT acknowledge funding from the Research Council of Finland (grant number 330165; 337552357904; 359342 and 359196). We acknowledge Erkka Rinne and the Ministry of Transport and Communications through the Integrated Carbon Observing System (ICOS) research and ICOS Finland for the Sodankylä fAPAR data, and in-situ observations. We thank Dr. Maiju Linkosalmi for the Sodankylä in-situ leaf-chlchlleaf. We also acknowledge Pablo Reyes-Muñoz for providing the Sentinel-3 OLCI remote sensing chlleaf data for the Sodankylä and Niwot Ridge sites. We thank Prof. Gab Abramowitz for the PLUMBER2 data. In addition, the authors thank Gabriela Sophia and Dr. Manon Sabot for helping to retrieve data from the TRY database. The authors also thank the QUINCY scientific programmers Dr. Jan Engel and Dr. Julia Nabel for technical support. For computing resources, we acknowledge Max Planck Institute for Biogeochemistry.

1090

- Abramowitz, G., Ukkola, A., Hobeichi, S., Cranko Page, J., Lipson, M., De Kauwe, M. G., Green, S., Brenner, C., Frame, J., Nearing, G., Clark, M., Best, M., Anthoni, P., Arduini, G., Boussetta, S., Caldararu, S., Cho, K., Cuntz, M., Fairbairn, D., Ferguson, C. R., Kim, H., Kim, Y., Knauer, J., Lawrence, D., Luo, X., Malyshev, S., Nitta, T., Ogee, J., Oleson, K., Ottlé, C., Peylin, P., de Rosnay, P., Rumbold, H., Su, B., Vuichard, N., Walker, A. P., Wang-Faivre, X., Wang, Y., and Zeng, Y.: On the predictability of turbulent fluxes from land: PLUMBER2 MIP experimental description and preliminary results. Biogeosciences, 21, 5517–5538, https://doi.org/10.5194/bg-21-5517-2024, 2024.
- Arora, V. K., Katavouta, A., Williams, R. G., Jones, C. D., Brovkin, V., Friedlingstein, P., Schwinger, J., Bopp, L., Boucher, O., Cadule, P., Chamberlain, M. A., Christian, J. R., Delire, C., Fisher, R. A., Hajima, T., Ilyina, T., Joetzjer, E., Kawamiya, M., Koven, C. D., Krasting, J. P., Law, R. M., Lawrence, D. M., Lenton, A., Lindsay, K., Pongratz, J., Raddatz, T., Séférian, R., Tachiiri, K., Tjiputra, J. F., Wiltshire, A., Wu, T., and Ziehn, T.: Carbon–concentration and carbon–climate feedbacks in CMIP6 models and their comparison to CMIP5 models, Biogeosciences, 17, 4173–4222, https://doi.org/10.5194/bg-17-4173-2020, 2020.
- Baret, F., Weiss, M., Lacaze, R., Camacho, F., Makhmara, H., Pacholcyzk, P., and Smets, B.: GEOV1: LAI and FAPAR essential climate variables and FCOVER global time series capitalizing over existing products. Part1: Principles of development and production, Remote Sensing of Environment, 137, 299–309, https://doi.org/10.1016/j.rse.2012.12.027, 2013.
- Best, M. J., Pryor, M., Clark, D. B., Rooney, G. G., Essery, R. L. H., Ménard, C. B., Edwards, J. M., Hendry, M. A., Porson, A., Gedney, N., Mercado, L. M., Sitch, S., Blyth, E., Boucher, O., Cox, P. M., Grimmond, C. S. B., and Harding, R. J.: The Joint UK Land Environment Simulator (JULES), model description Part 1: Energy and water fluxes, Geoscientific Model Development, 4, 677–699, https://doi.org/10.5194/gmd-4-677-2011, 2011.
  - Blyth, E. M., Arora, V. K., Clark, D. B., Dadson, S. J., De Kauwe, M. G., Lawrence, D. M., Melton, J. R., Pongratz, J., Turton, R. H., Yoshimura, K., and Yuan, H.: Advances in land surface modelling, Current Climate Change Reports, 7, 45–71, https://doi.org/10.1007/s40641-021-00171-5, 2021.
  - Boegh, E., Houborg, R., Bienkowski, J., Braban, C. F., Dalgaard, T., van Dijk, N., Dragosits, U., Holmes, E., Magliulo, V., Schelde, K., Di Tommasi, P., Vitale, L., Theobald, M. R., Cellier, P., and Sutton, M. A.: Remote sensing of LAI, chlorophyll and leaf nitrogen pools of crop- and grasslands in five European landscapes, Biogeosciences, 10, 6279–6307, https://doi.org/10.5194/bg-10-6279-2013, 2013.
- Bonan, G. B., Lawrence, P. J., Oleson, K. W., Levis, S., Jung, M., Reichstein, M., Lawrence, D. M., and Swenson, S. C.: Improving canopy processes in the Community Land Model version 4 (CLM4) using global flux fields empirically inferred from FLUXNET data, Journal of Geophysical Research: Biogeosciences, 116, https://doi.org/10.1029/2010JG001593, 2011.
  - Bowling, D. and Logan, B.: Conifer Needle Pigment Composition, Niwot Ridge, Colorado, USA, 2017-2018, https://doi.org/10.3334/ORNLDAAC/1723, last access: February 17, 2025, 2019.
- Bowling, D. R., Logan, B. A., Hufkens, K., Aubrecht, D. M., Richardson, A. D., Burns, S. P., Anderegg, W. R., Blanken, P. D., and Eiriksson,
  D. P.: Limitations to winter and spring photosynthesis of a Rocky Mountain subalpine forest, Agricultural and Forest Meteorology, 252,
  241–255, https://doi.org/10.1016/j.agrformet.2018.01.025, 2018.
  - Breiman, L.: Random forests, Machine Learning, 45, 5–32, https://doi.org/10.1023/A:1010933404324, 2001.
  - Caldararu, S., Thum, T., Yu, L., and Zaehle, S.: Whole-plant optimality predicts changes in leaf nitrogen under variable CO<sub>2</sub> and nutrient availability, New Phytologist, 225, 2331–2346, https://doi.org/10.1111/nph.16327, 2020.
- 1115 Caldararu, S., Thum, T., Yu, L., Kern, M., Nair, R., and Zaehle, S.: Long-term ecosystem nitrogen limitation from foliar δ15N data and a land surface model, Global Change Biology, 28, 493–508, https://doi.org/10.1111/gcb.15933, 2022.

- Chen, J. and Leblanc, S.: A four-scale bidirectional reflectance model based on canopy architecture, IEEE Transactions on Geoscience and Remote Sensing, 35, 1316–1337, https://doi.org/10.1109/36.628798, 1997.
- Clark, D. B., Mercado, L. M., Sitch, S., Jones, C. D., Gedney, N., Best, M. J., Pryor, M., Rooney, G. G., Essery, R. L. H., Blyth, E., Boucher,
  O., Harding, R. J., Huntingford, C., and Cox, P. M.: The Joint UK Land Environment Simulator (JULES), model description Part 2:
  Carbon fluxes and vegetation dynamics, Geoscientific Model Development, 4, 701–722, https://doi.org/10.5194/gmd-4-701-2011, 2011.
  - Collier, N., Hoffman, F. M., Lawrence, D. M., Keppel-Aleks, G., Koven, C. D., Riley, W. J., Mu, M., and Randerson, J. T.: The International Land Model Benchmarking (ILAMB) System: Design, Theory, and Implementation, Journal of Advances in Modeling Earth Systems, 10, 2731–2754. https://doi.org/10.1029/2018MS001354. 2018.
- 1125 Croft, H. and Chen, J.: 3.09 Leaf Pigment Content, in: Comprehensive Remote Sensing, edited by Liang, S., pp. 117–142, Elsevier, Oxford, https://doi.org/10.1016/B978-0-12-409548-9.10547-0, 2018.
  - Croft, H., Chen, J. M., Luo, X., Bartlett, P., Chen, B., and Staebler, R. M.: Leaf chlorophyll content as a proxy for leaf photosynthetic capacity, Global Change Biology, 23, 3513–3524, https://doi.org/10.1111/gcb.13599, 2017.
- Croft, H., Chen, J., Wang, R., Mo, G., Luo, S., Luo, X., He, L., Gonsamo, A., Arabian, J., Zhang, Y., Simic-Milas, A., Noland, T., He, Y.,

  Homolová, L., Malenovský, Z., Yi, Q., Beringer, J., Amiri, R., Hutley, L., Arellano, P., Stahl, C., and Bonal, D.: The global distribution of leaf chlorophyll content. Remote Sensing of Environment, 236, 111 479, https://doi.org/10.1016/j.rse.2019.111479, 2020.
  - Davies-Barnard, T. and Friedlingstein, P.: The global distribution of biological nitrogen fixation in terrestrial natural ecosystems, Global Biogeochemical Cycles, 34, e2019GB006 387, https://doi.org/10.1029/2019GB006387, 2020.
- Davies-Barnard, T., Meyerholt, J., Zaehle, S., Friedlingstein, P., Brovkin, V., Fan, Y., Fisher, R. A., Jones, C. D., Lee, H., Peano, D., Smith,

  B., Wårlind, D., and Wiltshire, A. J.: Nitrogen cycling in CMIP6 land surface models: progress and limitations, Biogeosciences, 17,

  5129–5148, https://doi.org/10.5194/bg-17-5129-2020, 2020.
  - Dechant, B., Kattge, J., Pavlick, R., Schneider, F. D., Sabatini, F. M., Moreno-Martínez, Á., Butler, E. E., van Bodegom, P. M., Vallicrosa, H., Kattenborn, T., Boonman, C. C., Madani, N., Wright, I. J., Dong, N., Feilhauer, H., Peñuelas, J., Sardans, J., Aguirre-Gutiérrez, J., Reich, P. B., Leitão, P. J., Cavender-Bares, J., Myers-Smith, I. H., Durán, S. M., Croft, H., Prentice, I. C., Huth, A., Rebel, K., Zaehle, S.,
- Šímová, I., Díaz, S., Reichstein, M., Schiller, C., Bruelheide, H., Mahecha, M., Wirth, C., Malhi, Y., and Townsend, P. A.: Intercomparison of global foliar trait maps reveals fundamental differences and limitations of upscaling approaches, Remote Sensing of Environment, 311, 114 276, https://doi.org/10.1016/j.rse.2024.114276, 2024.

- Demmig-Adams, B., Koh, S.-C., Cohu, C. M., Muller, O., Stewart, J. J., and Adams, W. W.: Non-photochemical fluorescence quenching in contrasting plant species and environments, in: Non-photochemical quenching and energy dissipation in plants, algae and cyanobacteria, edited by Demmig-Adams, B., Garab, G., Adams III, W., and Govindjee, pp. 531–552, Springer Netherlands, Dordrecht, https://doi.org/10.1007/978-94-017-9032-1\_24, 2014.
- ESA: Land Cover CCI Product User Guide Version 2. Tech. Rep., maps.elie.ucl.ac.be/CCI/viewer/download/ESACCI-LC-Ph2-PUGv2\_2.0. pdf, last access: February 12, 2025, 2017.
- Evans, J. R.: Photosynthesis and nitrogen relationships in leaves of C3 plants, Oecologia, 78, 9–19, https://doi.org/10.1007/BF00377192, 1150 1989.
  - Evans, J. R. and Clarke, V. C.: The nitrogen cost of photosynthesis, Journal of Experimental Botany, 70, 7–15, https://doi.org/10.1093/jxb/ery366, 2018.
  - Evans, J. R. and Clarke, V. C.: The nitrogen cost of photosynthesis, Journal of Experimental Botany, 70, 7–15, https://doi.org/10.1093/jxb/ery366, 2019.

- 1155 Famiglietti, C. A., Smallman, T. L., Levine, P. A., Flack-Prain, S., Quetin, G. R., Meyer, V., Parazoo, N. C., Stettz, S. G., Yang, Y., Bonal, D., Bloom, A. A., Williams, M., and Konings, A. G.: Optimal model complexity for terrestrial carbon cycle prediction, Biogeosciences, 18, 2727–2754, https://doi.org/10.5194/bg-18-2727-2021, 2021.
- Fang, H., Jiang, C., Li, W., Wei, S., Baret, F., Chen, J. M., Garcia-Haro, J., Liang, S., Liu, R., Myneni, R. B., Pinty, B., Xiao, Z., and Zhu, Z.: Characterization and intercomparison of global moderate resolution leaf area index (LAI) products: Analysis of climatologies and theoretical uncertainties, Journal of Geophysical Research: Biogeosciences, 118, 529–548, https://doi.org/10.1002/jgrg.20051, 2013.
  - Farella, M. M., Barnes, M. L., Breshears, D. D., Mitchell, J., van Leeuwen, W. J. D., and Gallery, R. E.: Evaluation of vegetation indices and imaging spectroscopy to estimate foliar nitrogen across disparate biomes, Ecosphere, 13, e3992, https://doi.org/10.1002/ecs2.3992, 2022.
    - Farquhar, G. D., von Caemmerer, S., and Berry, J. A.: A biochemical model of photosynthetic CO<sub>2</sub> assimilation in leaves of C3 species, Planta, 149, 78–90, https://doi.org/10.1007/BF00386231, 1980.
- 1165 Fisher, J. B., Badgley, G., and Blyth, E.: Global nutrient limitation in terrestrial vegetation, Global Biogeochemical Cycles, 26, https://doi.org/10.1029/2011GB004252, 2012.
  - Fisher, R. A. and Koven, C. D.: Perspectives on the future of land surface models and the challenges of representing complex terrestrial systems, Journal of Advances in Modeling Earth Systems, 12, e2018MS001453, https://doi.org/10.1029/2018MS001453, e2018MS001453 2018MS001453, 2020.
- 1170 FLUXNET: La Thuile Synthesis Dataset, FLUXNET [data set], https://fluxnet.org/data/la-thuile-dataset/, last access: Februrary 12, 2025, 2024.
  - Forrester, D. I., Bonal, D., Dawud, S., Gessler, A., Granier, A., Pollastrini, M., and Grossiord, C.: Drought responses by individual tree species are not often correlated with tree species diversity in European forests, Journal of Applied Ecology, 53, 1725–1734, https://doi.org/10.1111/1365-2664.12745, 2016.
- Friedlingstein, P., Jones, M. W., O'Sullivan, M., Andrew, R. M., Hauck, J., Peters, G. P., Peters, W., Pongratz, J., Sitch, S., Le Quéré, C., Bakker, D. C. E., Canadell, J. G., Ciais, P., Jackson, R. B., Anthoni, P., Barbero, L., Bastos, A., Bastrikov, V., Becker, M., Bopp, L., Buitenhuis, E., Chandra, N., Chevallier, F., Chini, L. P., Currie, K. I., Feely, R. A., Gehlen, M., Gilfillan, D., Gkritzalis, T., Goll, D. S., Gruber, N., Gutekunst, S., Harris, I., Haverd, V., Houghton, R. A., Hurtt, G., Ilyina, T., Jain, A. K., Joetzjer, E., Kaplan, J. O., Kato, E., Klein Goldewijk, K., Korsbakken, J. I., Landschützer, P., Lauvset, S. K., Lefèvre, N., Lenton, A., Lienert, S., Lombardozzi, D., Marland,
- G., McGuire, P. C., Melton, J. R., Metzl, N., Munro, D. R., Nabel, J. E. M. S., Nakaoka, S.-I., Neill, C., Omar, A. M., Ono, T., Peregon, A., Pierrot, D., Poulter, B., Rehder, G., Resplandy, L., Robertson, E., Rödenbeck, C., Séférian, R., Schwinger, J., Smith, N., Tans, P. P., Tian, H., Tilbrook, B., Tubiello, F. N., van der Werf, G. R., Wiltshire, A. J., and Zaehle, S.: Global Carbon Budget 2019, Earth System Science Data, 11, 1783–1838, https://doi.org/10.5194/essd-11-1783-2019, 2019.

Friedlingstein, P., O'Sullivan, M., Jones, M. W., Andrew, R. M., Bakker, D. C. E., Hauck, J., Landschützer, P., Le Quéré, C., Luijkx, I. T.,

Hurtt, G. C., Iida, Y., Ilyina, T., Jacobson, A. R., Jain, A., Jarníková, T., Jersild, A., Jiang, F., Jin, Z., Joos, F., Kato, E., Keeling, R. F.,

- Peters, G. P., Peters, W., Pongratz, J., Schwingshackl, C., Sitch, S., Canadell, J. G., Ciais, P., Jackson, R. B., Alin, S. R., Anthoni, P., Barbero, L., Bates, N. R., Becker, M., Bellouin, N., Decharme, B., Bopp, L., Brasika, I. B. M., Cadule, P., Chamberlain, M. A., Chandra, N., Chau, T.-T.-T., Chevallier, F., Chini, L. P., Cronin, M., Dou, X., Enyo, K., Evans, W., Falk, S., Feely, R. A., Feng, L., Ford, D. J., Gasser, T., Ghattas, J., Gkritzalis, T., Grassi, G., Gregor, L., Gruber, N., Gürses, Ö., Harris, I., Hefner, M., Heinke, J., Houghton, R. A.,
- 1190 Kennedy, D., Klein Goldewijk, K., Knauer, J., Korsbakken, J. I., Körtzinger, A., Lan, X., Lefèvre, N., Li, H., Liu, J., Liu, Z., Ma, L., Marland, G., Mayot, N., McGuire, P. C., McKinley, G. A., Meyer, G., Morgan, E. J., Munro, D. R., Nakaoka, S.-I., Niwa, Y., O'Brien, K. M., Olsen, A., Omar, A. M., Ono, T., Paulsen, M., Pierrot, D., Pocock, K., Poulter, B., Powis, C. M., Rehder, G., Resplandy, L.,

- Robertson, E., Rödenbeck, C., Rosan, T. M., Schwinger, J., Séférian, R., Smallman, T. L., Smith, S. M., Sospedra-Alfonso, R., Sun, Q., Sutton, A. J., Sweeney, C., Takao, S., Tans, P. P., Tian, H., Tilbrook, B., Tsujino, H., Tubiello, F., van der Werf, G. R., van Ooijen, E.,
- Wanninkhof, R., Watanabe, M., Wimart-Rousseau, C., Yang, D., Yang, X., Yuan, W., Yue, X., Zaehle, S., Zeng, J., and Zheng, B.: Global Carbon Budget 2023, Earth System Science Data, 15, 5301–5369, https://doi.org/10.5194/essd-15-5301-2023, 2023.
  - Friend, A., Stevens, A., Knox, R., and Cannell, M.: A process-based, terrestrial biosphere model of ecosystem dynamics (Hybrid v3.0), Ecological Modelling, 95, 249–287, https://doi.org/10.1016/S0304-3800(96)00034-8, 1997.
- Friend, A. D., Geider, R. J., Behrenfeld, M. J., and Still, C. J.: Photosynthesis in global-scale models, in: Photosynthesis in silico: Understanding complexity from molecules to ecosystems, edited by Laisk, A., Nedbal, L., and Govindjee, pp. 465–497, Springer Netherlands, Dordrecht, https://doi.org/10.1007/978-1-4020-9237-4 20, 2009.
  - Georgievski, G. and Hagemann, S.: Characterizing uncertainties in the ESA-CCI land cover map of the epoch 2010 and their impacts on MPI-ESM climate simulations, Theoretical and Applied Climatology, 137, 1587–1603, https://doi.org/10.1007/s00704-018-2675-2, 2019.
- Giannico, V., Chen, J., Shao, C., Ouyang, Z., John, R., and Lafortezza, R.: Contributions of landscape heterogeneity within the footprint of eddy-covariance towers to flux measurements, Agricultural and Forest Meteorology, 260-261, 144–153, https://doi.org/10.1016/j.agrformet.2018.06.004, 2018.
  - Griebel, A., Bennett, L. T., Metzen, D., Cleverly, J., Burba, G., and Arndt, S. K.: Effects of inhomogeneities within the flux footprint on the interpretation of seasonal, annual, and interannual ecosystem carbon exchange, Agricultural and Forest Meteorology, 221, 50–60, https://doi.org/10.1016/j.agrformet.2016.02.002, 2016.
- 1210 Harris, C.: CRU JRA v2.1: A forcings dataset of gridded land surfaceblend of Climatic Research Unit (CRU) and Japanese reanalysis (JRA) data, centre for Environmental Data Analysis, 2020.
  - Hastie, T., Tibshirani, R., and Friedman, J.: The elements of statistical learning: Data mining, inference, and prediction, Second Edition., vol. Second edition, corrected 7th printing of *Springer Series in Statistics*, Springer, 2009.
  - Heiskanen, J., Rautiainen, M., Stenberg, P., Mõttus, M., Vesanto, V.-H., Korhonen, L., and Majasalmi, T.: Seasonal variation in MODIS LAI for a boreal forest area in Finland, Remote Sensing of Environment, 126, 104–115, https://doi.org/10.1016/j.rse.2012.08.001, 2012.

- Hengl, T., Mendes de Jesus, J., Heuvelink, G. B. M., Ruiperez Gonzalez, M., Kilibarda, M., Blagotić, A., Shangguan, W., Wright, M. N., Geng, X., Bauer-Marschallinger, B., Guevara, M. A., Vargas, R., MacMillan, R. A., Batjes, N. H., Leenaars, J. G. B., Ribeiro, E., Wheeler, I., Mantel, S., and Kempen, B.: SoilGrids250m: Global gridded soil information based on machine learning, PLOS ONE, 12, 1–40, https://doi.org/10.1371/journal.pone.0169748, 2017.
- Houborg, R., Cescatti, A., Migliavacca, M., and Kustas, W.: Satellite retrievals of leaf chlorophyll and photosynthetic capacity for improved modeling of GPP, Agricultural and Forest Meteorology, 177, 10–23, https://doi.org/10.1016/j.agrformet.2013.04.006, 2013.
  - Howell, T., Meek, D., and Hatfield, J.: Relationship of photosynthetically active radiation to shortwave radiation in the San Joaquin Valley, Agricultural Meteorology, 28, 157–175, https://doi.org/10.1016/0002-1571(83)90005-5, 1983.
- Isaac, P., Cleverly, J., McHugh, I., van Gorsel, E., Ewenz, C., and Beringer, J.: OzFlux data: network integration from collection to curation, Biogeosciences, 14, 2903–2928, https://doi.org/10.5194/bg-14-2903-2017, 2017.
  - Jacquemoud, S. and Baret, F.: PROSPECT: A model of leaf optical properties spectra, Remote Sensing of Environment, 34, 75–91, https://doi.org/10.1016/0034-4257(90)90100-Z, 1990.
  - Joshi, R. K., Gupta, R., Mishra, A., and Garkoti, S. C.: Seasonal variations of leaf ecophysiological traits and strategies of co-occurring evergreen and deciduous trees in white oak forest in the central Himalaya, Environmental Monitoring and Assessment, 196, 634, https://doi.org/10.1007/s10661-024-12771-3, 2024.

- Katahata, S.-I., Naramoto, M., Kakubari, Y., and Mukai, Y.: Seasonal changes in photosynthesis and nitrogen allocation in leaves of different ages in evergreen understory shrub Daphniphyllum humile, Trees, 21, 619–629, https://doi.org/10.1007/s00468-007-0155-x, 2007.
- Kattge, J., Díaz, S., Lavorel, S., Prentice, I. C., Leadley, P., Bönisch, G., Garnier, E., Westoby, M., Reich, P. B., Wright, I. J., Cornelissen, J. H. C., Violle, C., Harrison, S. P., Van Bodegom, P. M., Reichstein, M., Enquist, B. J., Soudzilovskaia, N. A., Ackerly, D. D., Anand,
- M., Atkin, O., Bahn, M., Baker, T. R., Baldocchi, D., Bekker, R., Blanco, C. C., Blonder, B., Bond, W. J., Bradstock, R., Bunker, D. E., Casanoves, F., Cavender-bares, J., Chambers, J. Q., Chapin Iii, F. S., Chave, J., Coomes, D., Cornwell, W. K., Craine, J. M., Dobrin, B. H., Duarte, L., Durka, W., Elser, J., Esser, G., Estiarte, M., Fagan, W. F., Fang, J., Fernández-méndez, F., Fidelis, A., Finegan, B., Flores, O., Ford, H., Frank, D., Freschet, G. T., Fyllas, N. M., Gallagher, R. V., Green, W. A., Gutierrez, A. G., Hickler, T., Higgins, S. I., Hodgson, J. G., Jalili, A., Jansen, S., Joly, C. A., Kerkhoff, A. J., Kirkup, D., Kitajima, K., Klever, M., Klotz, S., Knops, J. M. H., Kramer, K.,
- Kühn, I., Kurokawa, H., Laughlin, D., Lee, T. D., Leishman, M., Lens, F., Lenz, T., Lewis, S. L., Lloyd, J., Llusiá, J., Louault, F., Ma, S., Mahecha, M. D., Manning, P., Massad, T., Medlyn, B. E., Messier, J., Moles, A. T., Müller, S. C., Nadrowski, K., Naeem, S., Niinemets, Ü., Nöllert, S., Nüske, A., Ogaya, R., Oleksyn, J., Onipchenko, V. G., Onoda, Y., Ordoñez, J., Overbeck, G., Ozinga, W. A., Patiño, S., Paula, S., Pausas, J. G., Peñuelas, J., Phillips, O. L., Pillar, V., Poorter, H., Poorter, L., Poschlod, P., Prinzing, A., Proulx, R., Rammig, A., Reinsch, S., Reu, B., Sack, L., Salgado-negret, B., Sardans, J., Shiodera, S., Shipley, B., Siefert, A., Sosinski, E., Soussana, J.-f., Swaine,
- E., Swenson, N., Thompson, K., Thornton, P., Waldram, M., Weiher, E., White, M., White, S., Wright, S. J., Yguel, B., Zaehle, S., Zanne, A. E., and Wirth, C.: TRY a global database of plant traits, Global Change Biology, 17, 2905–2935, https://doi.org/10.1111/j.1365-2486.2011.02451.x, 2011.
  - Kern, M. A.: Nitrogen controls on plant carbon-use efficiency, Ph.D. thesis, TUM school of life sciences, Technical University of Munich, https://pure.mpg.de/rest/items/item\_3356842\_3/component/file\_3362059/content, last access: February 17, 2025, 2021.
- 1250 Knohl, A. and Baldocchi, D. D.: Effects of diffuse radiation on canopy gas exchange processes in a forest ecosystem, Journal of Geophysical Research: Biogeosciences, 113, https://doi.org/10.1029/2007JG000663, 2008.
  - Knorr, W., Williams, M., Thum, T., Kaminski, T., Voßbeck, M., Scholze, M., Quaife, T., Smallman, T. L., Steele-Dunne, S. C., Vreugdenhil, M., Green, T., Zaehle, S., Aurela, M., Bouvet, A., Bueechi, E., Dorigo, W., El-Madany, T. S., Migliavacca, M., Honkanen, M., Kerr, Y. H., Kontu, A., Lemmetyinen, J., Lindqvist, H., Mialon, A., Miinalainen, T., Pique, G., Ojasalo, A., Ouegan, S., Rayner, P. J., Reyes-Muñoz, P.
- Rodríguez-Fernández, N., Schwank, M., Verrelst, J., Zhu, S., Schüttemeyer, D., and Drusch, M.: A comprehensive land-surface vegetation model for multi-stream data assimilation, D&B v1.0, Geoscientific Model Development, 18, 2137–2159, https://doi.org/10.5194/gmd-18-2137-2025, 2025.
  - Kooistra, L., Berger, K., Brede, B., Graf, L. V., Aasen, H., Roujean, J.-L., Machwitz, M., Schlerf, M., Atzberger, C., Prikaziuk, E., Ganeva, D., Tomelleri, E., Croft, H., Reyes-Muñoz, P., Garcia Millan, V., Darvishzadeh, R., Koren, G., Herrmann, I., Rozenstein, O., Belda, S.,
- Rautiainen, M., Rune Karlsen, S., Figueira Silva, C., Cerasoli, S., Pierre, J., Tanır Kayıkçı, E., Halabuk, A., Tunc Gormus, E., Fluit, F., Cai, Z., Kycko, M., Udelhoven, T., and Verrelst, J.: Reviews and syntheses: Remotely sensed optical time series for monitoring vegetation productivity, Biogeosciences, 21, 473–511, https://doi.org/10.5194/bg-21-473-2024, 2024.

- Kou-Giesbrecht, S., Arora, V. K., Seiler, C., Arneth, A., Falk, S., Jain, A. K., Joos, F., Kennedy, D., Knauer, J., Sitch, S., O'Sullivan, M., Pan, N., Sun, Q., Tian, H., Vuichard, N., and Zaehle, S.: Evaluating nitrogen cycling in terrestrial biosphere models: a disconnect between the carbon and nitrogen cycles, Earth System Dynamics, 14, 767–795, https://doi.org/10.5194/esd-14-767-2023, 2023.
- Krinner, G., Viovy, N., de Noblet-Ducoudré, N., Ogée, J., Polcher, J., Friedlingstein, P., Ciais, P., Sitch, S., and Prentice, I. C.: A dynamic global vegetation model for studies of the coupled atmosphere-biosphere system, Global Biogeochemical Cycles, 19, https://doi.org/10.1029/2003GB002199, 2005.

- Kull, O. and Kruijt, B.: Leaf photosynthetic light response: A mechanistic model for scaling photosynthesis to leaves and canopies, Functional Ecology, 12, 767–777, http://www.jstor.org/stable/2390464, 1998.
  - Laitinen, K., Luomala, E.-M., Kellomäki, S., and Vapaavuori, E.: Carbon assimilation and nitrogen in needles of fertilized and unfertilized field-grown Scots pine at natural and elevated concentrations of CO<sub>2</sub>, Tree Physiology, 20, 881–892, https://doi.org/10.1093/treephys/20.13.881, 2000.
- Lamarque, J.-F., Bond, T. C., Eyring, V., Granier, C., Heil, A., Klimont, Z., Lee, D., Liousse, C., Mieville, A., Owen, B., Schultz, M. G.,
  Shindell, D., Smith, S. J., Stehfest, E., Van Aardenne, J., Cooper, O. R., Kainuma, M., Mahowald, N., McConnell, J. R., Naik, V., Riahi,
  K., and van Vuuren, D. P.: Historical (1850–2000) gridded anthropogenic and biomass burning emissions of reactive gases and aerosols:
  methodology and application, Atmospheric Chemistry and Physics, 10, 7017–7039, https://doi.org/10.5194/acp-10-7017-2010, 2010.

1285

- Lamarque, J.-F., Kyle, G. P., Meinshausen, M., Riahi, K., Smith, S. J., van Vuuren, D. P., Conley, A. J., and Vitt, F.: Global and regional evolution of short-lived radiatively-active gases and aerosols in the Representative Concentration Pathways, Climatic Change, 109, 191, https://doi.org/10.1007/s10584-011-0155-0, 2011.
- LeBauer, D. S. and Treseder, K. K.: Nitrogen limitation of net primary productivity in terrestrial ecosystems is globally distributed, Ecology, 89, 371–379, https://esajournals.onlinelibrary.wiley.com/doi/abs/10.1890/06-2057.1, 2008.
- Legner, N.: Spatial variation of photosynthetic capacity of early-, mid-, or late-successional broad-leaved tree species in a temperate mixed forest, Ph.D. thesis, Georg August University of Göttingen, https://ediss.uni-goettingen.de/handle/11858/00-1735-0000-0012-DD8F-B, last access April 2, 2025, 2012.
- Linkosalmi, M., Aurela, M., Tuovinen, J.-P., Peltoniemi, M., Tanis, C. M., Arslan, A. N., Kolari, P., Böttcher, K., Aalto, T., Rainne, J., Hatakka, J., and Laurila, T.: Digital photography for assessing the link between vegetation phenology and CO<sub>2</sub> exchange in two contrasting northern ecosystems, Geoscientific Instrumentation, Methods and Data Systems, 5, 417–426, https://doi.org/10.5194/gi-5-417-2016, 2016.
- Liu, Y., Chen, J. M., He, L., Wang, R., Smith, N. G., Keenan, T. F., Rogers, C., Li, W., and Leng, J.: Global photosynthetic capacity of C3 biomes retrieved from solar-induced chlorophyll fluorescence and leaf chlorophyll content, Remote Sensing of Environment, 287, 113 457, https://doi.org/10.1016/j.rse.2023.113457, 2023.
  - Lu, X., Ju, W., Li, J., Croft, H., Chen, J. M., Luo, Y., Yu, H., and Hu, H.: Maximum carboxylation rate estimation with chlorophyll content as a proxy of Rubisco content, Journal of Geophysical Research: Biogeosciences, 125, e2020JG005748, https://doi.org/10.1029/2020JG005748, e2020JG005748 2020JG005748, 2020.
- Lu, X., Croft, H., Chen, J. M., Luo, Y., and Ju, W.: Estimating photosynthetic capacity from optimized Rubisco-chlorophyll relation-ships among vegetation types and under global change, Environmental Research Letters, 17, 014 028, https://doi.org/10.1088/1748-9326/ac444d, 2022.
  - Lundberg, S. M. and Lee, S.-I.: A unified approach to interpreting model predictions, in: Advances in neural information processing systems 30, edited by Guyon, I., Luxburg, U. V., Bengio, S., Wallach, H., Fergus, R., Vishwanathan, S., and Garnett, R., pp. 4765–4774, Curran Associates, Inc., http://papers.nips.cc/paper/7062-a-unified-approach-to-interpreting-model-predictions.pdf, 2017.
  - Luo, X., Croft, H., Chen, J. M., Bartlett, P., Staebler, R., and Froelich, N.: Incorporating leaf chlorophyll content into a two-leaf terrestrial biosphere model for estimating carbon and water fluxes at a forest site, Agricultural and Forest Meteorology, 248, 156–168, https://doi.org/10.1016/j.agrformet.2017.09.012, 2018.
- Luo, X., Croft, H., Chen, J. M., He, L., and Keenan, T. F.: Improved estimates of global terrestrial photosynthesis using information on leaf chlorophyll content, Global Change Biology, 25, 2499–2514, https://doi.org/10.1111/gcb.14624, 2019.

- Luo, X., Keenan, T. F., Chen, J. M., Croft, H., Colin Prentice, I., Smith, N. G., Walker, A. P., Wang, H., Wang, R., Xu, C., and Zhang, Y.: Global variation in the fraction of leaf nitrogen allocated to photosynthesis, Nature Communications, 12, 4866, https://doi.org/10.1038/s41467-021-25163-9, 2021.
- Medlyn, B. E., Zaehle, S., De Kauwe, M. G., Walker, A. P., Dietze, M. C., Hanson, P. J., Hickler, T., Jain, A. K., Luo, Y., Parton, W., Prentice,

  I. C., Thornton, P. E., Wang, S., Wang, Y.-P., Weng, E., Iversen, C. M., McCarthy, H. R., Warren, J. M., Oren, R., and Norby, R. J.: Using ecosystem experiments to improve vegetation models, Nature Climate Change, 5, 528–534, https://doi.org/10.1038/nclimate2621, 2015.
  - Meyerholt, J., Zaehle, S., and Smith, M. J.: Variability of projected terrestrial biosphere responses to elevated levels of atmospheric CO<sub>2</sub> due to uncertainty in biological nitrogen fixation, Biogeosciences, 13, 1491–1518, https://doi.org/10.5194/bg-13-1491-2016, 2016.
- Meyerholt, J., Sickel, K., and Zaehle, S.: Ensemble projections elucidate effects of uncertainty in terrestrial nitrogen limitation on future carbon uptake, Global Change Biology, 26, 3978–3996, https://doi.org/10.1111/gcb.15114, 2020.
  - Miinalainen, T. and Thum, T.: Data for the manuscript 'Evaluating the carbon and nitrogen cycles of the QUINCY terrestrial biosphere model using remotely-sensed data', Finnish Meteorological Institute, https://doi.org/10.57707/FMI-B2SHARE.6A3849A7694B4F4A9EFBA39ABDE734AF, 2025.
- Miinalainen, T., Thum, T., Aurela, M., and Croft, H.: Data for the manuscript 'Evaluating the carbon and nitrogen cycles of the QUINCY ter-1320 restrial biosphere model using space-born optical remotely-sensed data', Finnish Meteorological Institute, https://doi.org/10.57707/FMI-B2SHARE.F8AB5F4ED6534B1597A2DB73CC5175FF, 2025.
  - Nabuurs, G.-J., Mrabet, R., Hatab, A. A., Bustamante, M., Clark, H., Havlík, P., House, J., Mbow, C., Ninan, K., Popp, A., Roe, S., Sohngen, B., and Towprayoo, S.: Agriculture, Forestry and Other Land Uses (AFOLU), in: Climate Change 2022: Mitigation of Climate Change. Contribution of Working Group III to the Sixth Assessment Report of the Intergovernmental Panel on Climate Change, edited by Shukla,
- P., Skea, J., Slade, R., Khourdajie, A. A., van Diemen, R., McCollum, D., Pathak, M., Some, S., Vyas, P., Fradera, R., Belkacemi, M., Hasija, A., Lisboa, G., Luz, S., and Malley, J., book section 7, Cambridge University Press, Cambridge, UK and New York, NY, USA, https://doi.org/10.1017/9781009157926.009, 2022.
  - Niinemets, Ü., Kull, O., and Tenhunen, J. D.: An analysis of light effects on foliar morphology, physiology, and light interception in temperate deciduous woody species of contrasting shade tolerance, Tree Physiology, 18, 681–696, https://doi.org/10.1093/treephys/18.10.681, 1998.
- Onoda, Y., Wright, I. J., Evans, J. R., Hikosaka, K., Kitajima, K., Niinemets, Ü., Poorter, H., Tosens, T., and Westoby, M.: Physiological and structural tradeoffs underlying the leaf economics spectrum, New Phytologist, 214, 1447–1463, https://doi.org/10.1111/nph.14496, 2017.
  - Parton, W. J., Scurlock, J. M. O., Ojima, D. S., Gilmanov, T. G., Scholes, R. J., Schimel, D. S., Kirchner, T., Menaut, J.-C., Seastedt, T., Garcia Moya, E., Kamnalrut, A., and Kinyamario, J. I.: Observations and modeling of biomass and soil organic matter dynamics for the grassland biome worldwide, Global Biogeochemical Cycles, 7, 785–809, https://doi.org/10.1029/93GB02042, 1993.
- Pastorello, G., Trotta, C., Canfora, E., Chu, H., Christianson, D., Cheah, Y.-W., Poindexter, C., Chen, J., Elbashandy, A., Humphrey, M., Isaac, P., Polidori, D., Reichstein, M., Ribeca, A., van Ingen, C., Vuichard, N., Zhang, L., Amiro, B., Ammann, C., Arain, M. A., Ardö, J., Arkebauer, T., Arndt, S. K., Arriga, N., Aubinet, M., Aurela, M., Baldocchi, D., Barr, A., Beamesderfer, E., Marchesini, L. B., Bergeron, O., Beringer, J., Bernhofer, C., Berveiller, D., Billesbach, D., Black, T. A., Blanken, P. D., Bohrer, G., Boike, J., Bolstad, P. V., Bonal, D., Bonnefond, J.-M., Bowling, D. R., Bracho, R., Brodeur, J., Brümmer, C., Buchmann, N., Burban, B., Burns, S. P., Buysse, P., Cale, P.,
- Cavagna, M., Cellier, P., Chen, S., Chini, I., Christensen, T. R., Cleverly, J., Collalti, A., Consalvo, C., Cook, B. D., Cook, D., Coursolle, C., Cremonese, E., Curtis, P. S., D'Andrea, E., da Rocha, H., Dai, X., Davis, K. J., Cinti, B. D., Grandcourt, A. d., Ligne, A. D., De Oliveira, R. C., Delpierre, N., Desai, A. R., Di Bella, C. M., Di Tommasi, P., Dolman, H., Domingo, F., Dong, G., Dore, S., Duce, P., Dufrêne, E., Dunn, A., Dušek, J., Eamus, D., Eichelmann, U., ElKhidir, H. A. M., Eugster, W., Ewenz, C. M., Ewers, B., Famulari, D., Fares, S.,

- Feigenwinter, I., Feitz, A., Fensholt, R., Filippa, G., Fischer, M., Frank, J., Galvagno, M., Gharun, M., Gianelle, D., Gielen, B., Gioli, B.,
- 1345 Gitelson, A., Goded, I., Goeckede, M., Goldstein, A. H., Gough, C. M., Goulden, M. L., Graf, A., Griebel, A., Gruening, C., Grünwald,
- T., Hammerle, A., Han, S., Han, X., Hansen, B. U., Hanson, C., Hatakka, J., He, Y., Hehn, M., Heinesch, B., Hinko-Najera, N., Hörtnagl,
  - L., Hutley, L., Ibrom, A., Ikawa, H., Jackowicz-Korczynski, M., Janouš, D., Jans, W., Jassal, R., Jiang, S., Kato, T., Khomik, M., Klatt,
    - J., Knohl, A., Knox, S., Kobayashi, H., Koerber, G., Kolle, O., Kosugi, Y., Kotani, A., Kowalski, A., Kruijt, B., Kurbatova, J., Kutsch,
    - W. L., Kwon, H., Launiainen, S., Laurila, T., Law, B., Leuning, R., Li, Y., Liddell, M., Limousin, J.-M., Lion, M., Liska, A. J., Lohila,
- A., López-Ballesteros, A., López-Blanco, E., Loubet, B., Loustau, D., Lucas-Moffat, A., Lüers, J., Ma, S., Macfarlane, C., Magliulo, V.,
  - Maier, R., Mammarella, I., Manca, G., Marcolla, B., Margolis, H. A., Marras, S., Massman, W., Mastepanov, M., Matamala, R., Matthes,
  - J. H., Mazzenga, F., McCaughey, H., McHugh, I., McMillan, A. M. S., Merbold, L., Meyer, W., Meyers, T., Miller, S. D., Minerbi, S.,
  - Moderow, U., Monson, R. K., Montagnani, L., Moore, C. E., Moors, E., Moreaux, V., Moureaux, C., Munger, J. W., Nakai, T., Neirynck,
  - J., Nesic, Z., Nicolini, G., Noormets, A., Northwood, M., Nosetto, M., Nouvellon, Y., Novick, K., Oechel, W., Olesen, J. E., Ourcival,
  - J.-M., Papuga, S. A., Parmentier, F.-J., Paul-Limoges, E., Pavelka, M., Peichl, M., Pendall, E., Phillips, R. P., Pilegaard, K., Pirk, N.,
    - Posse, G., Powell, T., Prasse, H., Prober, S. M., Rambal, S., Rannik, Ü., Raz-Yaseef, N., Rebmann, C., Reed, D., Dios, V. R. d., Restrepo-Coupe, N., Reverter, B. R., Roland, M., Sabbatini, S., Sachs, T., Saleska, S. R., Sánchez-Cañete, E. P., Sanchez-Mejia, Z. M., Schmid,

    - H. P., Schmidt, M., Schneider, K., Schrader, F., Schroder, I., Scott, R. L., Sedlák, P., Serrano-Ortíz, P., Shao, C., Shi, P., Shironya, I.,
    - Siebicke, L., Šigut, L., Silberstein, R., Sirca, C., Spano, D., Steinbrecher, R., Stevens, R. M., Sturtevant, C., Suyker, A., Tagesson, T.,
- Takanashi, S., Tang, Y., Tapper, N., Thom, J., Tomassucci, M., Tuovinen, J.-P., Urbanski, S., Valentini, R., van der Molen, M., van Gorsel,
  - E., van Huissteden, K., Varlagin, A., Verfaillie, J., Vesala, T., Vincke, C., Vitale, D., Vygodskaya, N., Walker, J. P., Walter-Shea, E., Wang,
  - H., Weber, R., Westermann, S., Wille, C., Wofsy, S., Wohlfahrt, G., Wolf, S., Woodgate, W., Li, Y., Zampedri, R., Zhang, J., Zhou, G.,
  - Zona, D., Agarwal, D., Biraud, S., Torn, M., and Papale, D.: The FLUXNET2015 dataset and the ONEFlux processing pipeline for eddy
  - covariance data, Scientific Data, 7, 225, https://doi.org/10.1038/s41597-020-0534-3, 2020.
- Pedregosa, F., Varoquaux, G., Gramfort, A., Michel, V., Thirion, B., Grisel, O., Blondel, M., Prettenhofer, P., Weiss, R., Dubourg, V., Vanderplas, J., Passos, A., Cournapeau, D., Brucher, M., Perrot, M., and Duchesnay, E.: Scikit-learn: Machine Learning in Python, Journal
  - of Machine Learning Research, 12, 2825–2830, 2011.

- Peltoniemi, M., Ruhanen, H., Linkosalmi, M., and Aurela, M.: Shoot pigment measurements from Scots pine trees at the Sodankylä eddy
  - covariance site in 2015, https://doi.org/10.5281/zenodo.17192030, 2025.
- 1370 Rastetter, E. B., Vitousek, P. M., Field, C. B., Shaver, G. R., Herbert, D. A., and Gren, G. I.: Resource optimization and symbiotic nitrogen
- fixation, Ecosystems, 4, 369–388, https://doi.org/10.1007/s10021-001-0018-z, 2001.
- Reves-Muñoz, P., Pipia, L., Salinero-Delgado, M., Belda, S., Berger, K., Estévez, J., Morata, M., Rivera-Caicedo, J. P., and Verrelst, J.:
  - Quantifying fundamental vegetation traits over Europe using the Sentinel-3 OLCI Catalogue in Google Earth Engine, Remote Sensing,
    - 14, https://doi.org/10.3390/rs14061347, 2022.
- 1375 Rogers, A., Medlyn, B. E., Dukes, J. S., Bonan, G., von Caemmerer, S., Dietze, M. C., Kattge, J., Leakey, A. D. B., Mercado, L. M.,
  - Niinemets, Ü., Prentice, I. C., Serbin, S. P., Sitch, S., Way, D. A., and Zaehle, S.: A roadmap for improving the representation of photo
    - synthesis in Earth system models, New Phytologist, 213, 22-42, https://doi.org/10.1111/nph.14283, 2017.
    - Sage, R. F., Pearcy, R. W., and Seemann, J. R.: The nitrogen use efficiency of C3 and C4 plants: III. Leaf nitrogen effects on the
- activity of carboxylating enzymes in Chenopodium album (L.) and Amaranthus retroflexus (L.), Plant Physiology, 85, 355-359,
- 1380 https://doi.org/10.1104/pp.85.2.355, 1987.

- Sallas, L., Luomala, E.-M., Utriainen, J., Kainulainen, P., and Holopainen, J. K.: Contrasting effects of elevated carbon dioxide concentration and temperature on Rubisco activity, chlorophyll fluorescence, needle ultrastructure and secondary metabolites in conifer seedlings, Tree Physiology, 23, 97–108, https://doi.org/10.1093/treephys/23.2.97, 2003.
- Seiler, C., Kou-Giesbrecht, S., Arora, V. K., and Melton, J. R.: The impact of climate forcing biases and the nitrogen cycle on land carbon balance projections, Journal of Advances in Modeling Earth Systems, 16, e2023MS003749, https://doi.org/10.1029/2023MS003749, e2023MS003749 2023MS003749, 2024.
  - Stenberg, P., DeLucia, E. H., Schoettle, A. W., and Smolander, H.: Photosynthetic light capture and processing from cell to canopy, in: Resource physiology of conifers, acquition, allocation, and utilization, edited by Smith, W. K. and Hinckley, T. M., pp. 3–38, Academic Press, 3rd edn., 1995.
- 1390 Tamm, C. O.: Nitrogen-Limited and Nitrogen-Depleted Terrestrial Ecosystems: Ecological Characteristics, in: Nitrogen in Terrestrial Ecosystems: Questions of Productivity, Vegetational Changes, and Ecosystem Stability, pp. 34–49, Springer Berlin Heidelberg, Berlin, Heidelberg, https://doi.org/10.1007/978-3-642-75168-4\_3, 1991.
  - Thomas, R. Q., Brookshire, E. N. J., and Gerber, S.: Nitrogen limitation on land: how can it occur in Earth system models?, Global Change Biology, 21, 1777–1793, https://doi.org/10.1111/gcb.12813, 2015.
- Thum, T., Aalto, T., Laurila, T., Aurela, M., Kolari, P., and Hari, P.: Parametrization of two photosynthesis models at the canopy scale in a northern boreal Scots pine forest, Tellus B: Chemical and Physical Meteorology, https://doi.org/10.1111/j.1600-0889.2007.00305.x, 2007.
  - Thum, T., Caldararu, S., Engel, J., Kern, M., Pallandt, M., Schnur, R., Yu, L., and Zaehle, S.: A new model of the coupled carbon, nitrogen, and phosphorus cycles in the terrestrial biosphere (QUINCY v1.0; revision 1996), Geoscientific Model Development, 12, 4781–4802, https://doi.org/10.5194/gmd-12-4781-2019, 2019.
- Thum, T., Miinalainen, T., Seppälä, O., Croft, H., Rogers, C., Staebler, R., Caldararu, S., and Zaehle, S.: Modelling decadal trends and the impact of extreme events on carbon fluxes in a temperate deciduous forest using a terrestrial biosphere model, Biogeosciences, 22, 1781–1807, https://doi.org/10.5194/bg-22-1781-2025, 2025.

- Thurner, M., Yu, K., Manzoni, S., Prokushkin, A., Thurner, M. A., Wang, Z., and Hickler, T.: Nitrogen concentrations in boreal and temperate tree tissues vary with tree age/size, growth rate, and climate, Biogeosciences, 22, 1475–1493, https://doi.org/10.5194/bg-22-1475-2025, 2025.
- Tum, M., Günther, K. P., Böttcher, M., Baret, F., Bittner, M., Brockmann, C., and Weiss, M.: Global Gap-Free MERIS LAI Time Series (2002–2012), Remote Sensing, 8, https://doi.org/10.3390/rs8010069, 2016.
- Ukkola, A. M., Abramowitz, G., and De Kauwe, M. G.: A flux tower dataset tailored for land model evaluation, Earth System Science Data, 14, 449–461, https://doi.org/10.5194/essd-14-449-2022, 2022.
- 1410 Verhoef, W.: Light scattering by leaf layers with application to canopy reflectance modeling: The SAIL model, Remote Sensing of Environment, 16, 125–141, https://doi.org/10.1016/0034-4257(84)90057-9, 1984.
  - Vicente-Serrano, S. M., Domínguez-Castro, F., Reig, F., Tomas-Burguera, M., Peña-Angulo, D., Latorre, B., Beguería, S., Rabanaque, I., Noguera, I., Lorenzo-Lacruz, J., and El Kenawy, A.: A global drought monitoring system and dataset based on ERA5 reanalysis: A focus on crop-growing regions, Geoscience Data Journal, 10, 505–518, https://doi.org/10.1002/gdj3.178, 2023.
- 1415 Vitousek, P. M. and Howarth, R. W.: Nitrogen limitation on land and in the sea: How can it occur?, Biogeochemistry, 13, 87–115, https://doi.org/10.1007/BF00002772, 1991.

- Vuichard, N., Messina, P., Luyssaert, S., Guenet, B., Zaehle, S., Ghattas, J., Bastrikov, V., and Peylin, P.: Accounting for carbon and nitrogen interactions in the global terrestrial ecosystem model ORCHIDEE (trunk version, rev 4999): multi-scale evaluation of gross primary production, Geoscientific Model Development, 12, 4751–4779, https://doi.org/10.5194/gmd-12-4751-2019, 2019.
- 1420 Wang, C., Yang, Y., Yin, G., Xie, Q., Xu, B., Verger, A., Descals, A., Filella, I., and Peñuelas, J.: Divergence in autumn phenology extracted from different satellite proxies reveals the timetable of leaf senescence over deciduous forests, Geophysical Research Letters, 51, e2023GL107 346, https://doi.org/10.1029/2023GL107346, e2023GL107346 2023GL107346, 2024.

- Wang, R., Chen, J. M., Luo, X., Black, A., and Arain, A.: Seasonality of leaf area index and photosynthetic capacity for better estimation of carbon and water fluxes in evergreen conifer forests, Agricultural and Forest Meteorology, 279, 107708, https://doi.org/10.1016/j.agrformet.2019.107708, 2019.
- Warren, C. R. and Adams, M. A.: Distribution of N, Rubisco and photosynthesis in Pinus pinaster and acclimation to light, Plant, Cell & Environment, 24, 597–609, https://doi.org/10.1046/j.1365-3040.2001.00711.x, 2001.
- Wellburn, A. R.: The Spectral Determination of Chlorophylls a and b, as well as Total Carotenoids, Using Various Solvents with Spectrophotometers of Different Resolution, Journal of Plant Physiology, 144, 307–313, https://doi.org/10.1016/S0176-1617(11)81192-2, 1994.
- 1430 Wullschleger, S. D.: Biochemical limitations to carbon assimilation in C3 plants—A retrospective analysis of the A/Ci curves from 109 species, Journal of Experimental Botany, 44, 907–920, https://doi.org/10.1093/jxb/44.5.907, 1993.
  - Yasumura, Y. and Ishida, A.: Temporal variation in leaf nitrogen partitioning of a broad-leaved evergreen tree, Quercus myrsinaefolia, Journal of Plant Research, 124, 115–123, https://doi.org/10.1007/s10265-010-0358-x, 2011.
  - Zaehle, S. and Friend, A. D.: Carbon and nitrogen cycle dynamics in the O-CN land surface model: 1. Model description, site-scale evaluation, and sensitivity to parameter estimates, Global Biogeochemical Cycles, 24, https://doi.org/10.1029/2009GB003521, 2010.
    - Zaehle, S., Medlyn, B. E., De Kauwe, M. G., Walker, A. P., Dietze, M. C., Hickler, T., Luo, Y., Wang, Y.-P., El-Masri, B., Thornton, P., Jain, A., Wang, S., Warlind, D., Weng, E., Parton, W., Iversen, C. M., Gallet-Budynek, A., McCarthy, H., Finzi, A., Hanson, P. J., Prentice, I. C., Oren, R., and Norby, R. J.: Evaluation of 11 terrestrial carbon–nitrogen cycle models against observations from two temperate Free-Air CO<sub>2</sub> Enrichment studies, New Phytologist, 202, 803–822, https://doi.org/10.1111/nph.12697, 2014.
- Zhang, C., Atherton, J., Peñuelas, J., Filella, I., Kolari, P., Aalto, J., Ruhanen, H., Bäck, J., and Porcar-Castell, A.: Do all chlorophyll fluorescence emission wavelengths capture the spring recovery of photosynthesis in boreal evergreen foliage?, Plant, Cell & Environment, 42, 3264–3279, https://doi.org/10.1111/pce.13620, 2019.
  - Ziehn, T., Wang, Y.-P., and Huang, Y.: Land carbon-concentration and carbon-climate feedbacks are significantly reduced by nitrogen and phosphorus limitation, Environmental Research Letters, 16, 074 043, https://doi.org/10.1088/1748-9326/ac0e62, 2021.